Synthesis and Characterization of Organo Lead Halide Perovskite Absorber Layer under ambient conditions for Perovskite Solar Cells

By

Sabahat Andleeb

School of Chemical and Materials Engineering

National University of Sciences and Technology

2023

Synthesis and Characterization of Organo- Lead Halide Perovskite Light Absorber Under Ambient conditions for perovskite Solar Cells

Sabahat Andleeb

Reg.No:00000319260

This thesis is submitted as a partial fulfillment of the requirements for the degree of

MS in Nanoscience and engineering

Supervisor Name: Dr. Muhammad Talha Masood

School of Chemical and Materials Engineering (SCME)

National University of Sciences and Technology (NUST)

H-12 Islamabad, Pakistan

July, 2023

THESIS ACCEPTANCE CERTIFICATE

Certified that final copy of MS thesis written by Ms **Sabahat Andleeb** (Registration No 00000319260), of School of Chemical & Materials Engineering (SCME) has been vetted by undersigned, found complete in all respects as per NUST Statues/Regulations, is free of plagiarism, errors, and mistakes and is accepted as partial fulfillment for award of MS degree. It is further certified that necessary amendments as pointed out by GEC members of the scholar have also been incorporated in the said thesis.

Signature: _____

Name of Supervisor: **Dr Muhammad Talha Masood**

Date: 05/09/2023

Signature (HOD): _____

Date: 5/9/23

Signature (Dean/Principal): _____

Date: 6-9-23

Form TH-1
(Must be type written)

National University of Sciences & Technology (NUST)
MASTER'S THESIS WORK
Formulation of Guidance and Examination Committee (GEC)

Name: **Sabahat Andleeb**
Department: **SCME**
Credit Hour Completed: **24**

NUST Regn No: **319260**
Specialization: **Nanoscience and engineering**
CGPA: **3.19**

Course Work Completed

S/No	Code	Title	Core/Elective	CH	Grade
1	MSE-856	Nanomaterials and processing	Core	3	B
2	MSE-854	Characterization of Materials	Core	3	B+
3	NSE-813	Essential of Science and Engineering	Core	3	B
4	MSE-862	Electronic and magnetic materials	Elective	3	B+
5	NSE-812	Environmental Nanotechnology	Elective	3	B
6	MSE-952	Materials for biomedical Application	Elective	3	B+
7	NSE-941	Nanocomposite Materials	Elective	3	B
8	NSE-842	Nnaomaterials for energy applications	Elective	3	B
9	RM-898	Research Methodology	Elective	3	Q

Date: 11-10-2021

Student's Signature:

Thesis Committee

1. Name: **Dr. Muhammad Talha Masood (Supervisor)**
   Department: **Materials Engineering**
   Signature:

   Dr M Talha Masood
   Assistant Professor
   SCME, NUST, H-12, Islamabad

2. Name: **Dr. Sofia Javed (Co-Supervisor)**
   Department: **Materials Engineering**
   Signature:

3. Name: **Dr. Aftab Akram**
   Department: **Materials Engineering**
   Signature:

4. Name: **Dr. Mohsin Saleem**
   Department: **Materials Engineering**
   Signature:

6. Name: **Dr. Nadia Shahzad (External)**
   Department: **USP-CASE**
   Signature:

Date: 25/10/2021

Signature of Head of Department:

APPROVAL

Date: 25-10-2021

Dean/Principal

Distribution
1x copy to Exam Branch, Main Office NUST
1x copy to PGP Dte, Main Office NUST
1x copy to Exam branch, respective institute

School of Chemical and Materials Engineering (SCME) Sector H-12, Islamabad

National University of Sciences &Technology (NUST)

FORM TH-4

MASTER'S THESIS WORK

We hereby recommend that the dissertation prepared under our supervision by

Regn No & Name: **0000319260 Sabahat Andleeb**

Title: **Synthesis and characterization of Organo-Lead Halide perovskite absorber layer under ambient conditions for Perovskite solar cells.**

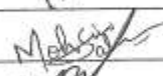Presented on: **30 Aug 2023**   at: **1400 hrs in SCME Seminar Hall**

Be accepted in partial fulfillment of the requirements for the award of Masters of Science degree in **Nanoscience & Engineering.**

Guidance & Examination Committee Members

Name: **Dr Nadia Shahzad** (USPCAS-E)   Signature: _____

Name: **Dr Mohsin Saleem**   Signature: _____

Name: **Dr M. Aftab Akram**   Signature: _____

Name: **Dr Sofia Javed** (Co-Supervisor)   Signature: _____

Supervisor's Name: **Dr M. Talha Masood**   Signature: _____

                                 Dated: 30/08/23

Head of Department   **Dean/Principal**

Date 31/08/2023   Date _____ 4-9-23

School of Chemical &Materials Engineering (SCME)

Dedication

This thesis is dedicated to my parents for their love, support, sacrifices, prayers, and advice.

Acknowledgments

Abstract

Perovskite solar cells are considered a promising material with the potential to create high performance solar cells at a low cost. They offer several advantages over many thin-film absorber layers, primarily because of their high absorption coefficient, tuneable band gap, ability to be processed at low temperature, and abundant availability of their elemental constituents. In this research study, the focus was on synthesizing $MAPbI_3$ perovskite-based absorber layer through a one-step antisolvent method. The aim of the study was to investigate the impact of different antisolvents, specifically chlorobenzene and toluene, on the crystallization process to achieve faster crystal growth. During the thin film formation, both chlorobenzene and toluene were employed as antisolvents. Comparative study conducted to understand the crystallization kinetics and film morphology .The results revealed that the choice of antisolvent had a remarkable effect on the crystallization rate of the perovskite. Faster crystal growth is observed while using toluene as antisolvent as compared to chlorobenzene .

The research also involved various characterizations, such as XRD, SEM, UV-Vis, FTIR, and Hall effect measurements. The purpose of characterization is to analyze the crystal structure, surface morphology, optical and electrical behavior of thin films.

Table of Contents

Table of Figures

Table of Tables

Abbreviations

ESL	Electron selective layer
HSL	Hole selective layer
PV	Photovoltaic
XRD	X-ray diffraction
SEM	Scanning electron microscopy.
FTIR	Fourier transform infra-red spectroscopy.
UV VIS	Ultraviolet visible spectroscopy
DMF	Dimethyl formamide
TL	Toluene
CB	Chlorobenzene
DMSO	Dimethyl sulfoxide
MAI	Methyl ammonium iodide

Chapter 1

Introduction

1.1. Background

Technological evolution has changed the social structure and living ways of individuals. Thus, being an important member of society, scientists must keep pace with all kinds of technological advancements and manage the information overload to make the maximum out of them. Despite a highly focused approach towards advancement in computer technology and artificial intelligence (AI), energy management at a global scale is still of maximum importance. This is because every technology, including AI, is energy dependent. However, the world's energy resources are shrinking day by day (such as fossil fuels) due to their overconsumption. Finite energy resources like coal and oil will eventually run out, which may result in severe energy crisis at global scale in near future. Combustion fossil fuels also release pollutants to the Earth's atmosphere, which contribute to climate change. Furthermore, electricity generation using hydel power plants has already disturbed the ecosystem of our planet (earth). Thus, it is important to shift towards renewable and clean energy resources to fulfill our daily industrial and domestic requirements. One of such renewable energy sources is our sun which exists at the very heart of our solar system. Converting solar energy from this gaseous star into the required forms (such as heat and electricity) is a clean and environmentally friendly process unlike burning fossil fuels and using hydel power plants.**[2]**

Many different types of renewable energy have their own advantages and disadvantages.   sophisticated systems are required to store and convert the prime type of energy into its required form. Such systems are called energy storage and conversion devices respectively. The energy storage devices store energy for further utilization in its useful form. Supercapacitors and batteries are the most common

energy storage device.[3] The **energy conversion devices** convert energy from one form into another. The solar cells and fuelcells are the most important examples.

The **solar cells** convert solar energy into electrical energy. This technology has immense potential to meet our energy requirements as alternative to electricity generated by power plants because it requires extensive infrastructure, high tension cables and regular maintenance.[4]

Silicon based solar cells are considered as technologically mature and reliable. However, there are some limitations associated with them, such as heavy weight,high fabrication cost due to energy and labor-intensive processes required for their manufacture at large-scale. Furthermore, having an indirect band gap semiconducting material silicon based photovoltaic devices cannot be synthesized as thin film devices (to cutdown material cost). To overcome these limitations, searches for alternative photovoltaic technology has increased. Therefore, solar cells have been categorized into three generations based on their structure, architecture, and type of absorbing materials. [5] These types of solar cells have been listed and explained below:

1.1.1 First generation solar cells

This comprises of diffused crystalline silicon to make a P-N junction diode. This is the oldest and most widely applied due to its reliability which developed over the years since 1950s. These devices are further categorized into single crystalline and polycrystalline solar cells. This, depends upon the manufacturing route followed for the silicon wafer fabrication. Although it costs less to produce polycrystalline silicon solar cells than single crystal ones, their performance is worse because grain boundaries create more resistance for the transportation of charge carriers across the material.[6] These devices are widely used across the world due to PCE of up to 27%, long term stability and technological maturity. Due to its indirect band gap semiconductor nature, crystalline silicon is widely manufactured in the form of wafers and is not utilized for flexible solar cells..[7]

Figure 1. 1. Solar panels based on crystalline Silicon wafers which are widely used. (First generation solar cells) [1]

1.1.2 Second generation solar cell

Second generation of solar cells were developed with the aim of reducing cost while minimizing the use of active material. This was done by bringing down the thickness photoactive material to few nanometers. In second-generation solar cells, photoactive materials for example amorphous silicon, cadmium telluride, and copper indium gallium selenide (CIGS) are applied onto the glass or flexible substrates. The power conversion efficiencies of these devices is reasonably high but inferior to that of first of generation solar cells.[8] Amorphous silicon based solar cells is commonly found in calculators and similar electronic applications which require less electrical power. Similarly, other second-generation solar cells are also used to power small-scale electrical appliances. However, toxicity associated with CIGS and CdTe limits their usage. Thus, further research was carried out towards third generation solar cells. [9]
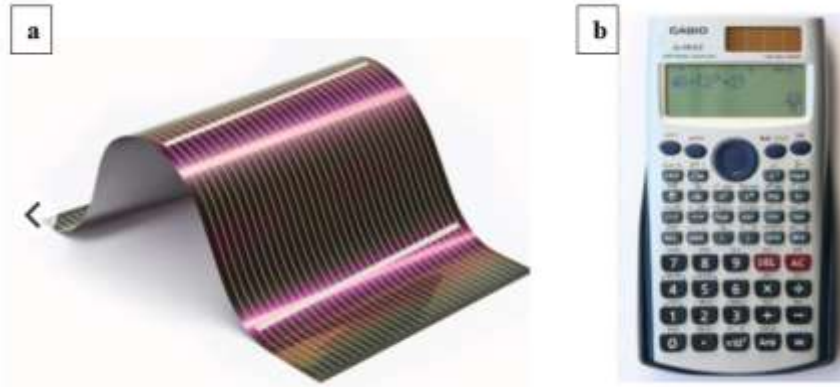
Figure 1. 2. Flexible their generation solar cells. (b). Amorphous Silicon based photovoltaic device integrated into electronic calculator.[10]

1.1.3. Third generation solar cells

These solar cells also comprise of thin films that can be fabricated on top of glass or flexible polymeric substrate [11]. However, their power conversion efficiencies are much higher compared to the second generation solar cells. Examples are DSSCs perovskites and organic solar cells. This generation of solar cells is still under research phase due to issues associated with their long-term stability. However, the bandgap of active material is tunable along with higher light harvesting compared to second generation solar cells from solar spectrum. Amongst all these PSCs are renowned in terms of high power conversion efficiencies. They are about to reach standard level of first generation [12]. The third generation of solar celss possess unique ability to work as solar window due to their transparency along with high external and internal quantum efficiency [13].

Figure 1. 3. Dye-sensitized solar cells as solar windows [14]

1.2. Perovskite solar cells (PSCs)

Perovskite solar cells (PSCs) are considered as a promising photovoltaic technology because of their low fabrication cost and impressive power conversion efficiencies. Moreover, their efficiency competes with silicon based solar cells. The pioneer PSC which was reported in 2009 had an efficiency of about 3.8 % [15]. Within less than a decade, the device performance surpassed 25% [16]. Efforts are underway to commercialize this as solar windows since it offers low fabrication cost (due to its solution-processability) and possibility to build device on top of glass substrates [17].

1.2.1. Working Principle and the most reported structures of Perovskite Solar Cells

The outstanding light harvesting properties of organo lead halide perovskite, which serves as photoactive layer provides the foundation for how PSCs function. Perovskite is sandwiched between HSL and ESL. When photoactive layer is illuminated with light, the electron and holes pairs are generated. Electrons will jump into the conduction band while holes will remain in the valence band. The ESL, (such as TiO_2) selectively extracts electrons which are subsequently sent to external circuit through TCO like fluorine doped tin oxide FTO or ITO. Conversely , holes are selectively

extracted by the hole selective layer HSL which include lithium doped spiro-OMeTAD).

Schematic of this process is explained in Fig 4 (a) and (b) for planar and mesostructured PSCs respectively. Here, the compact and/or mesostructured TiO_2 is shown as ESL. The perovskite/TiO_2 interfacial contact area is increased by adding mesoscopic TiO_2 layer on top of TiO_2 layer. The mesoscopic layer has remarkable effect of substantially increasing the number of nucleation sites for perovskite crystallization(see fig 4b). As a result, when the mesoscopic layer is present, electrons would be injected into the TiO2 nanostructure and subsequently into the compact TiO2 layer. It is widely reported that planar heterojunction architecture yields less PCEs and higher hysteresis in the J V curves while using TiO_2 as the ESL compared to mesoscopic PSCs. Hence , in some cases fabrication process of the active layer is not solution processed, such as vapor assisted method for perovskite deposition [18].

Fig 4c shows energy level alignment of perovskite working between different layers when light is absorbed by perovskite layer electrons will move from valance to conduction band leaving positively charged holes in the perovskite valance band. As the perovskite minimum of conduction is higher than that of ESL so electrons could be transferred to the conduction band of ESL. An electron injection barrier is caused by higher conduction band minimum of ESL compared to perovskite that can potentially decrease internal quantum efficiency. ESL is called a hole blocking layer since it prevents hole extraction from perovskite due to its high ionization energy relative to perovskite. On the contrary, the valence band maximum of the perovskite is lower than the HOMO level of the hole transport material. Therefore, holes from valence band of perovskite could be injected to valance band of HTM. So organo lead halide perovskite shows ambipolar character. On the other hand, the HSL must be made up of P type semiconductors while ESL must be ideally N type semiconductor (electrons are majority charge carriers). However, charge selectivity of respective contacts relies on the relative positions of their energy levels compared to perovskite layer at interface. It's the basic requirement for all hetero structure PV devices, but not an absolute rule.
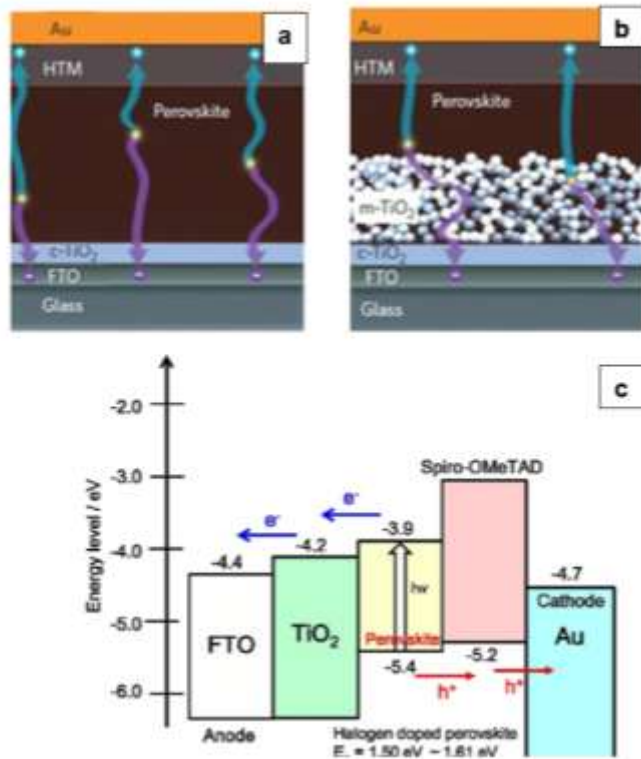
Figure 1. 4. Device architecture and working principle for (a). the planar heterojunction PSC, (b). the mesostructured PSCs[19] (c). Energy-level diagram explaining the working principle for a typical PSC device [20]
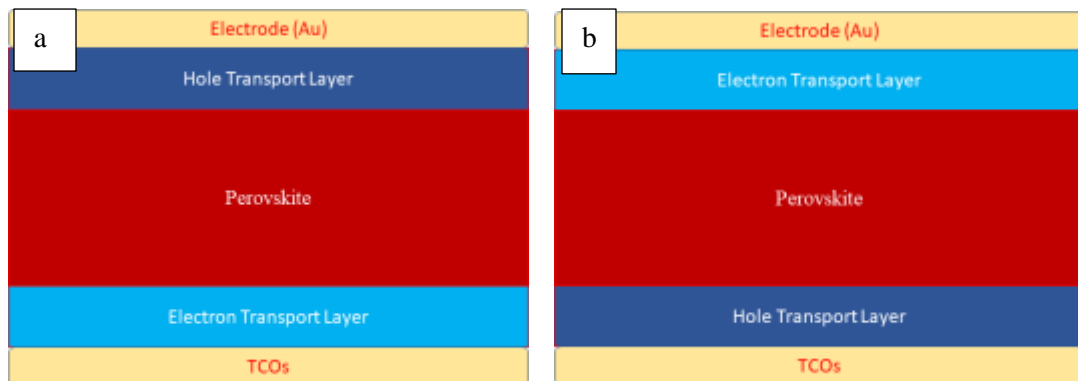
Figure 1. 5. Non-inverted n-i-p PSCs where the sequence of individual layers is TCO / ESL / Perovskite / HSL / Au (b). Inverted p-i-n inverted PSCs where the sequence of individual layers is TCO / HSL / Perovskite / ESL / Au

7

There is another way to categorize device structure i.e., based on the sequence or order in which ESL, the perovskite absorber and HSL are deposited. Here, the devices are categorized as n-i-p non-inverted or p-i-n inverted PSCs.

1.2.2. Components of Perovskite Solar Cells:

a. Transparent conductive metal oxide (TCO):

Fluorine doped Tin Oxide (FTO) and Indium doped Tin oxide (ITO) coated glass substrates are used. The entire device is coated on top of such transparent substrates. The sunlight enters the device from this part. Passing through the ESL (or HSL), it reaches the active layer (or absorber layer) which results in the production of photoinduced charge-carrier generation [21].

Perovskite light absorber:

Absorber layer actually having semiconductor material which is considered as heart of solar cell. In PVSCs, the perovskite layer play the role of absorber layer, its primary task is to absorb light and create free holes and electrons. Under the influence of electric field photogenerated carriers drift and diffuse. Electrons will migrate towards electron transport layer while holes will be extracted to hole transport layer. Efficiency of carrier extraction depends on the ability of transporting electron and hole carriers towards holes and electron transport layer respectively. Before returning to device at the opposite electrode and recombining with the hole, electrons and holes are caught by their respective electrodes, where they dissipate energy and produce electricity. If electrons are not extracted by ETL of perovskite, then it would recombine with holes [22].

Perovskite material offers more promising characteristics than traditional absorbers and dyes (which are frequently reported in (DSSCs) materials. Some of the most important characteristics are listed as follows:

i.   High carrier mobilities and diffusion lengths

ii.   High absorption coefficient

iii.   Low fabrication cost

v.   High photon to charge conversion efficiency

vi.   Low quality requirements of raw materials

vii.   Simple manufacturing process and low energy consumption

viii.   Transparent and flexible components can be prepared.

Some of these advantages are explained as follows:

i.   Low manufacturing cost

Low cost is the biggest advantage of perovskite solar cell duction both material and production cost. As cost of perovskite per square foot (0.09 square meter) is about $0.25, which almost one tenth of silicon based solar cell. Moreover, perovskite core raw material is not as much rare and supply in not as limited [23].

Other than that Perovskite films have high absorption coefficient about 100 times than traditional solar cells. Hence its film layer can be thinned which significantly reduces the material used for battery. (Crystalline silicon have thickness of about 160 to 180 μm whereases perovskite film thickness is typically only 0.3 to 0.5 μm. Statistically 35 kg of perovskite generates same amount of power of 7 tons of silicon. That is why the use of perovskite material has been reduced. Lastly low cost technology used to manufacture perovskite, that doesn't require expensive vacuum equipment [24].

ii.   High photoelectric conversion efficiency

The light absorption layer of perovskite solar cells have a wider band gap compared to crystalline silicon solar cells, enabling it to effectively capture short wavelength visible light. Simultaneously, Perovskite solar cell exhibit carrier mobility with remarkable light diffusion performance. Moreover, its electron and holes diffusion lengths can extend beyond 1000nm. In addition, perovskite's bandgap can be tuned by changing material of layer, which ultimately increases the photoelectric conversion efficiency of battery. Increasing band gap is also possible and can increase the conversion efficiency while stacking different layers of perovskite film. Photovoltaic efficiency of perovskite solar cells is rapidly increasing and is now close to 23%. Research from leading laboratories suggests that it could reach up to over 30% in the near future. This makes them ideal for solar energy conversion [25].

iii.   Low quality requirements of raw material

The synthesis of a perovskites does not require a high level of purity from the raw material and is not highly sensitive to any impurities within it. This allows for much more affordable and easier to source materials, making the entire process more cost-effective and efficient. A perovskite cell having purity of around 90% can be produced with an remarkable efficiency higher than 20% whereas silicon based cells require more purity like about 99.9999% [26].

iv.   Simple manufacturing process and low energy consumption

The manufacturing process of Perovskite is relatively simple and requires low energy consumption as compared to silicon based solar cells. It's usually made by mixing together organic cations, organic solvent, and inorganic halides. After the mixture is heated, Perovskite crystals can rapidly form. The entire process requires low cost of materials, low energy expenditure and is environmentally friendly [27].

v.   Transparent flexible components can be prepared.

The utilization of transparent flexible substrate perovskite battery allows manufacturing of flexible battery components. A variety of methos are being used for this purpose One popular method is to deposit layers of the perovskite material onto a substrate or substrate stack. This can involve physical or chemical vapor deposition, spin coating or even inkjet printing. Following deposition, the material is cured and then heat-treated to form the perovskite crystal structure. The cured material is then often recoated with a dielectric material to improve its optical and electrical properties. This one is utilized in unconventional applications such as glass curtains walls, sand portable products. Finally, it can be printed, cut and bent to desired shapes for use in a wide range of devices [28].

Contrary to it, there are some factors which limit the commercialization of Perovskites. The most important of such factors are listed as follows:

(i)   Poor structure stability

(ii)   Difficulty in large area preparation

(iii)   Environmental problems

(iv)   Ion migration

(v)   Metal contact corrosion

Some of these limitations are explained as follows:

i.   Poor structure stability

Instability of perovskite structure is actually because of instability of perovskite material itself and interface instability. Perovskite cell material is very sensitive to water and oxygen. Most commonly used material for hole transport also decomposes when used in moist environment.

Most commonly used TiO_2 (as an ESL) has photocatalytic properties, which accelerates photo-induced decomposition of perovskite when irradiated with sunlight. The 5% UV in the sunlight is responsible for such photocatalytic degradation processes (when TiO_2 is used). Therefore, the perovskite . Even though, irreversible structure changes occur which ultimately decreases performance, mainly moisture are prone to irreversible degradation .[29]

ii.   Difficulty in large area preparation (i.e., scalability)

It's pretty hard synthesis large area more efficient perovskite cells and to gain efficiency of more than 20% for single junction solar cell which exceeds about $1m^2$, as cell area increases the conversion efficiency will decrease. The reason for difficulty in large scale production is to get uniform and continuous coating for perovskite. Furthermore, TCO film have less resistance to collect current and when area will large its resistivity will become more obvious [30].

iii.   Environmental problems

Highly efficient perovskite solar cells material contains toxic metal such as lead, putting

a risk to health and environment. However, if amount of lead leakage is small it wouldn't have much effect on environmental toxicity. [31].

iv.   Ion Migration

During perovskite film formation degradation may occur due to creation of vacant vacancies. Vacancies can be of iodine or metal ion vacancies. Within lattice structure ion migration can be encouraged by these defects. Pin holes created in absorber layer due to ion migration which ultimately destroy crystal lattice structure and can affect cell performance. Probability of ion migration is like I- > MA+ > Pb2+. Ion migration is affected by surface boundaries and grain. Shows that grain size affects the extent of ion migration. So controlling grain size is crucial to control ion migration [32].

b.   Charge selective contacts (i.e., ESL and HSL):

The organo-lead halide is an excellent light harvesting material. It readily generates electron-hole pairs upon illumination with sunlight. However, the generation of these charge carriers is good for a successful photovoltaic device only if they are successfully extracted by the respective charge-selective contacts. Material characteristics, such as charge selectivity and majority charge carrier extraction capabilities, remarkably effects the choice of the most appropriate materials for charge extraction layers (or contacts) in a specific photovoltaic device. [33].

A contact must be selective to extract charge within single polarity while blocking opposite charges; that is termed as charge selectivity. A good PSC must have both ESL and HSL [34]. The energy level band alignment of ESL and HSL with light absorber material is crucial for the charge extraction and transport mechanisms. The accurate selection of ESLs and HSLs is important to avoid surface recombination, which would directly affect V_{OC} and FF .Here we will briefly discuss the ESL and the HSL [35].

Hole Selective Layer (HSL)

The fundamental principle which is applied is holes always flow from lower to higher energy level w.r.t to absorber layer while blocking electrons at that energy level. As long as the PSC's energy level architecture is strong enough, it can operate without an HTL.

However, an HTL that is suitable can improve cell performance. As it can transport holes from HOMO of absorber material to back metal contact electrode. It plays a crucial role in enhancing device stability while restricting direct contact between perovskite active layer and back metal contact electrode. A high quality HSL is necessary for effective hole extraction because it influence the Voc by specifying separation of quasi fermi energy level of Perovskite [36].

If there were no HSL, the back metal contact will directly deposit on perovskite which ultimately can degrade due to ionic nature of perovskite. Hence, the presence of HTL can cover perovskite, protect it from the environment, and prevent back contact from rusting. The selection of HSCs must meet several requirements, including strong chemical stability, high glass transition point, increased hole mobility, appropriate work function, and good transmission for usage in "p-i-n" structured devices. Spiro-OMeTAD have relatively less hole mobility [37].

Electron Selective Layer (ESL)

ESL is specifically used for extraction and transportation of photo-generated electrons from absorber layer of perovskite to TCO i.e., FTO or ITO while blocking holes from perovskite following the principle that electrons always flow from higher energy level to lower energy level w.r.t perovskite active layer. During extraction and transportation of electrons unwanted recombination can occur, that could be minimized while selecting proper ESL material [38].

The main attribute of the ETL is to fulfill band alignment with the perovskite layer and to possess high transmittance in the UV-Vis region, allowing photons to pass through and be absorbed by the perovskite active layer. Highly efficient ETLs must offer fast electron mobility to enable fast transportation from LOMO to conduction band of ETL. ETL can be organic or inorganic [39].

c. **Back metal Schottky contact:**

For efficient charge extraction of charge-carriers from other side, back metal contact is used. Gold [40], Silver [41], Aluminum [42], Copper [43]are the most reported back metal contacts.

1.3. Properties of organo-lead halide perovskite material

Perovskite belongs to class of material having an ABX_3 structure where A site cations are Methylammonium (MA^+, $CH_3NH_3^+$), Formamadium (FA^+, $CH(NH_2)_2^+$) and Cesium (Cs^+). B site cation is usually lead (II) (Pb^{2+}) and occasionally Tin (II) (Sn^{2+}); X site halides are Iodide (I^-), Bromide (Br^-) and Chloride (Cl^-) etc. The structure is shown in fig 1.6
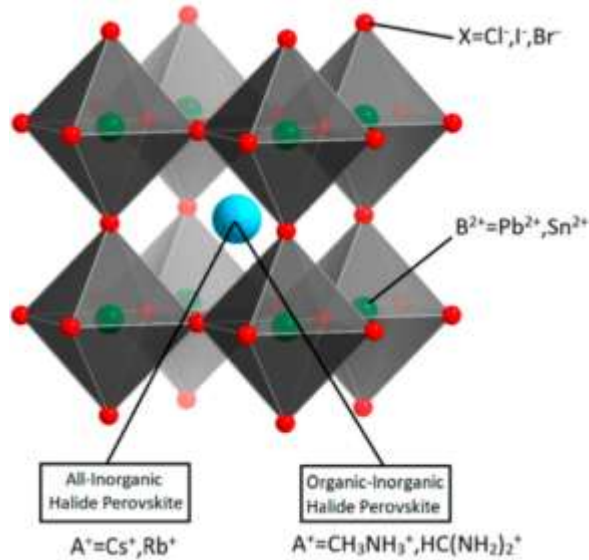
Figure 1. 6. Organo-lead halide perovskite structure, showing the A, B, and X positions with their corresponding ions [44]

Organo lead halide perovskite outstanding light harvesting material for photovoltaic applications due to its increased mobility, charge carrier lifetime and tunable band gap. Typical compositions of organo lead halide perovskite reported for solar applications are $FAPbI_3$, $CsPbI_3$ [45] methyl ammonium lead iodide $MAPbI_3$ [46], and mixed cation and anion lead halide perovskite [47] . Goldschmidt tolerance factor is used to find crystal structure which is calculated from ratio of ionic radii:

$$t = \frac{r_A + r_X}{\sqrt{2}(r_B + r_X)}$$

Here r_A , r_B and r_x represent ionic radii of A site cation, B site cation and X site halide anions. Perovskite structure is formed if the tolerance factor is between 0.71 and 1 [48].Within this range, the geometry of the perovskite varies depending upon the value of tolerance factor. For instance, between 0.91 to 1, perovskite becomes cubic while from 0.71 to 0.9, perovskite distorted into tetragonal form because of tilted [PbX$_6$] octahedras. Another common occurrence is that a particular perovskite material's crystal structure changes with temperature. For instance, MAPbI3 has a tolerance factor of 0.91, yet at room temperature, it is tetragonal rather than perfect cubic [49]. The tolerance factor for single cation FAPbI$_3$ is more than 1. Thus, it possesses a yellow non-photoactive phase and a hexagonal crystal shape at ambient temperature. With an orthorhombic structure and a tolerance factor under 0.8, CsPbI$_3$ is a yellow non photoactive phase. Nevertheless, the tolerance factor can be adjusted for stabilizing the black light alpha cubic phase to room temperature by adding the right amounts of MA$^+$ and/or Cs$^+$ cations to FAPbI$_3$ [50].

  It has been claimed that long term stability can be attained byusing double or triple cation perovskites (MA, FA, Cs) as light the harvest layer. TheGoldschmidt tolerance factor can be adjusted by replacing iodide with bromide, which improves stability [51]. The band gap of these perovskites can also be tuned by replacing iodide with bromide. The absorption edge of MAPbI$_3$ is at 780 nm, while MAPbBr$_3$is at 540 nm [52]. By raising the Br$^-$ ratio, the absorption edge of MAPbI$_3$ canbe proportionately blue shifted. Furthermore, the A site cation also alters the band gap. For instance, replacing the MA+ with FA+ can cause the absorption edge to be red shifted, which is what isseen in both iodide and bromide perovskites [53]. Steep PL emission following the absorption edge is also in literature, which allows for an efficient photon recycling, furtherverifying their excellent optical properties for PV applications [54].

1.4. Fabrication methods for perovskite active layer

Perovskite material can be synthesized by using various methos, including solution-based method. Whatever method is used for synthesis for perovskite material, but objective should be to control size and morphology.

1.4.1 Vapor deposition technique

It's a very popular method for synthesizing perovskite films. It involves heating and evaporating the desired precursor materials, which then react with a substrate surface to form a uniform and continuous film. The process allows for precise control over the composition and thickness of the resulting film, leading to improved performance in different applications including solar cells, LEDs, and sensors. However, technique requires careful optimization of deposition conditions to achieve optimal film quality and stability [55].
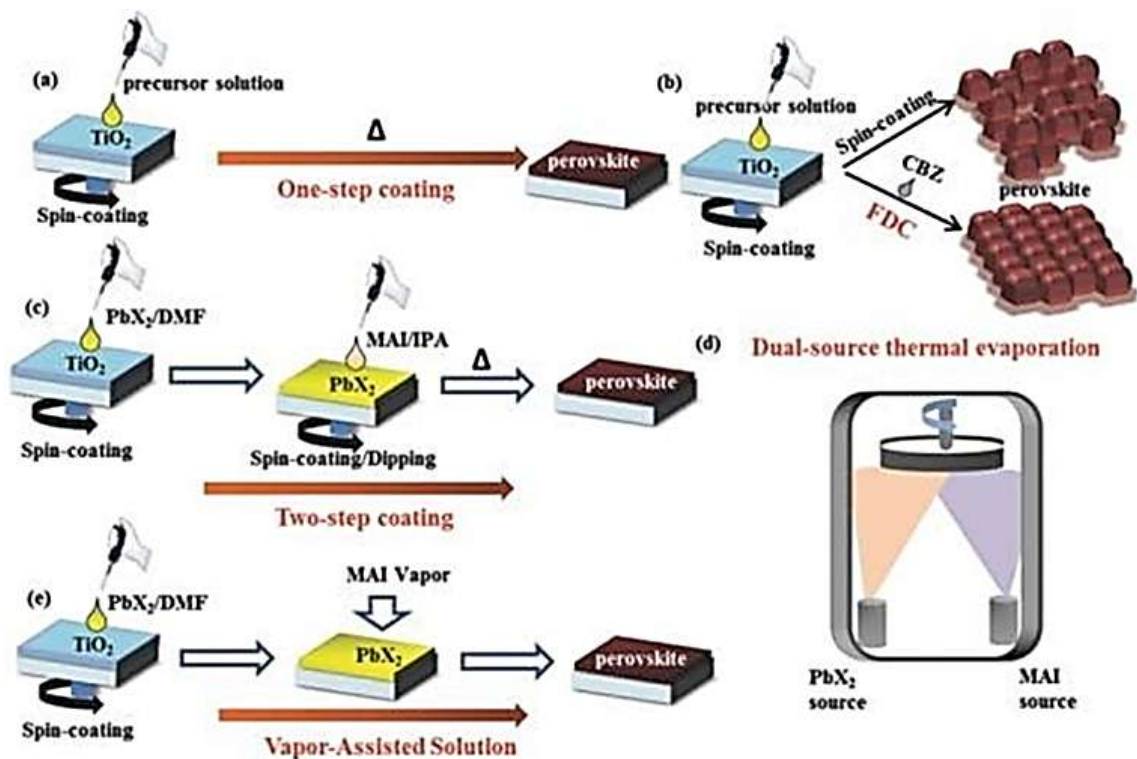
Figure 1. 7. (a) one step deposition (b) one step antisolvent deposition (c) Two step deposition (d) vapor assisted deposition [56]

1.4.2 Solution-processable techniques

For perovskite synthesis the most preferred method is solution based as its simplest and cost effective as well. Most effective solution-based method is spin-coating

deposition which is further divided in to two types:

(i) Two-step sequential deposition

Two step deposition is widely used for the manufacture of high quality perovskite films. With this method precursor solution containing lead iodide is spin coated on a suitable substrate followed closely by dipping [57] or spinning the monovalent organic cation precursor solution (e.g., MAI solution in propanol) on top of the rotating PbI_2 substrate [58].

(ii) Hot injection methods

In 2015 for the first time Kovalenko[58] *et al* used this method for synthesis of perovskite NCs. This method is more advantageous as it offers more control over morphology while delivering narrow size distribution and enabling fine tuning of material for optoelectronic applications. In this method, on the one hand at high temperature precursor solution is prepared in a 3-neck flask and at certain temperature second precursor would be injected by using a syringe into hot solution. Then growth and nucleation of NCs will start and then to stop growth process solution would be extinguished in ice bath after few seconds.[59]

(iii) One-step deposition

One-step deposition process for $MAPbI_3$ perovskite involves mixing the lead halide and organic precursor in a single solvent such as DMF or DMSO. The solution is to then spin coated on top of substrate MF and then spin coating the resulting solution ontoa suitable substrate. This method is in some way problematic because this results in incomplete coverage of perovskite active layer on top of the substrate. This is owing to the fact that DMF/DMSO solvents evaporate very slowly during spin coating. Thus, the crystallization of perovskite precursor is also non-uniform on the substrate surface. This results in the development of parallel shunts within the device which adversely influences the device's performance.

(iv)   One-step deposition using anti-solvent approach:

One-step deposition method was further improved by introducing anti-solvent approach to trigger quick evaporation of the solvent and uniform crystallization of the precursors and to ensure complete coverage on top of the substrate. In other words, to create a homogeneous, pinhole-free perovskite film, antisolvent treatment raises the nucleus density during film production. This results in perovskite films with low hysteresis and stability, which improves solar cell's power conversion efficiency. Different anti-solvents have been reported so far which includes chloroform [60], bromobenzene, toluene [61], diethyl ether, 1-3-methylImidazole iodized salt, and Chlorobenzene [62].

1.5 Aims and objectives.

The purpose of my research is:

- To Study the surface coverage of the organo-lead Halide perovskite ($CH_3NH_3PbI_3$, also known as $MAPbI_3$) on plane glass substrates.

- To Investigate the influence of two different anti-solvents (Chlorobenzene and Toluene) on thin film coverage by varying their application time.

- To investigate best results in terms of surface coverage achieved by applying Chlorobenzene and Toluene at different time intervals during the spin program.

- To investigate the optical properties of $MAPbI_3$ for perovskite solar cell applications.

Chapter 2

Literature Review

In this section, previously reported organo-lead halide perovskite (absorber) layer deposition studies will be discussed in detail. The discussion will be primarily based upon the issues, alternatives, and importance of anti-solvent. Earlier, the deposition of perovskite active layer was performed using one-step method (which has already been discussed in section 1.42). Unfortunately, the ultimate film is highly non-uniform in terms of surface coverage on top of the substrate. Detailed morphological studies have already pointed out the presence of large pinholes (or so called the isolated islands of perovskite layer on top of the substrate). The incomplete coverage of absorber layer (i.e., the perovskite) tends to allow direct parallel contact between the ESL and the HSL. Such defects are called parallel shunts which tends to reduce shunt resistance and deteriorate the device performance. To counter this issue, the mesoporous layer of TiO_2 was introduced to facilitate the crystallization of the absorber layer. The introduction of two-step sequential deposition further enhanced the morphology. However, the key issue with two-step deposition of perovskite was incomplete conversion of PbI_2 to $MAPbI_3$ (perovskite). Therefore, further advancement in one-step deposition was made by dropping an appropriate anti-solvent on top of substrate being spin-coated with single perovskite precursor solution. The perovskite precursor solution is based on a polar solvent for example DMF and DMSO. On the other hand, antisolvent which is dropped during the spin-coating program is highly non-polar (for instance Chlorobenzene or Toluene). The interaction between non-polar antisolvent and polar solvent renders quick evaporation and removal of solvent from the perovskite solution being spin-coated on top of the substrate. This prompts quick nucleation of perovskite precursor on top of the substrate to form uniform and pinhole free absorber layer on the substrate. In this research thesis, I studied the difference between the quality of perovskite ($MAPbI_3$) film on plane glass substrate when using two different ant-solvents (Chlorobenzene, and Toluene). Secondly, the film quality (in terms of crystallization and film morphology) was also investigated against time of

dropping the anti-solvent during spin-coating process.

In antisolvent drips process a predetermined amount of antisolvent is added. The time of dropping the antisolvent depends on the composition of precursor solution and the spin program. Upon dropping the anti-solvent, a spontaneous color change from yellow to dark orange is observed which is a sign of quick crystallization process. The perovskite is formed when the substrate is heated at around $100^{O}C$ for few minutes on hot plate. This process is done in an inert environment. However, in this research thesis, I have performed the perovskite deposition (with and without the use of an appropriate anti-solvent) under ambient conditions.

In one of the very earliest reports (in 2014) on antisolvent to the processing of perovskite layer, Xiao et al. explored a fast deposition crystallization (FDC) process using different antisolvents like chlorobenzene, benzene, toluene, xylene, methanol, 2-propanol etc. Among all antisolvents investigated, chlorobenzene, benzene, xylene, and toluene have been reported to achieve uniform and smooth films during the deposition process. Utilizing chlorobenzene as the antisolvent, the optimized devices with a perovskite layer thickness of 350 nm achieved a spectacular average power conversion efficiency (PCE) of 13.9%. This PCE exceeded efficiencies of perovskite solar cells obtained through other modern fabrication methods at that time [63].

Jeon et al. studied a miscible in DMF, DMSO, -butyrolactone GBLs, and others as antisolvents. To create the perovskite film, the $MAPb(I_{1-x} Br_x)_3$ perovskite precursors were coated onto a bilayer TiO_2 using a spin coating process tracked by toluene dripping and finally annealed at 100 °C for 10 mi The perovskite film obtained by using toluene dripping exhibited homogeneity, reduced roughness, and complete surface coverage. Perovskite solar cells manufactured using bilayer TiO2, a solvent mixture of GBL and DMSO, and toluene dripping achieved an average PCE of 16.5%. [64].

The rate of application of the anti-solvent itself is an important parameter which directly influences the film quality. First, if the anti-solvent is applied with a superfast

rate, the perovskite precursor solution is scrapped off the substrate. If it is applied at a very slow rate, other undesirable effects on the film quality is repeatedly observed. Jung et al studied this effect in detail. They not only studied 14 different anti-solvents, but also investigated the influence of the antisolvent application rate. Through the use of 14 different antisolvents, a comprehensive structural, compositional, and microstructural characterization has led to two important observations. First, the solubility of organic precursors in antisolvents and their miscibility with the host solvent are directly affected by the choice of the antisolvent. Thus, based on these attributes, the antisolvents have been classified into three different types:

TYPE I: Those that good for short application time,

TYPE II: Those that have no effect.

TYPE III: Those that perform better for longer application time.

It is worth noting that while considering fast versus slow application of antisolvent, the difference between antisolvents is quite apparent. **Type I** antisolvent (alcohol series ethyl, isopropyl, and butyl alcohols) shows better performance by adding antisolvent quickly while its slow application adversely affects the device performance. For **type III** anti solvent trend is exactly opposite. **Type II** anti-solvents do not influence the perovskite film quality and the device performance whether they are applied quickly or slowly.

Additionally employing the antisolvent technique for optimizing perovskite film morphology, studies have also reported the effect of precursor solution concentration and temperature on the film formation process. For instance, Alturisa et al [65] observed that utilizing a precursor solution at both 40°C and 60°C gave the formation of a mesh-like structure in the perovskite layer. However, the optimum temperature in order to achieve the highest conversion of precursor solution to perovskite, with a lower percentage of unconverted lead iodide is about 60°C. Similarly, the optimized concentration of precursor solution was found to 1.0M to render uniform active layer on top a given substrate.

To increase it is good to utilize appropriate methods to avoid degradation of perovskite active layer. There are three types of processes which render degradation of organo lead halide perovskite and leading to poor long term stability of the PSC. The degradation is induced by moisture, oxygen, heat and light. In many cases, all these three factors collectively work together to deteriorate the device performance which limits the use of PSC at commercial scale. Encapsulation of the PSC with epoxy of similar material have been used to avoid oxygen and moisture degradation of perovskite layer. Furthermore, Carbon electrodes have also been employed to encounter moisture induced degradation. To avoid light induced degradation, the composition of perovskite active layer and charge selective contacts were widely[66] studied . However, the long term stability of PSCs remains around 10,000 hours (i.e., 14 months). Apart from considering degradation of perovskite active layer, the long-term stability of hole transport layer has also been proposed by several researchers. The most commonly reported approach towards the stabilization of charge-selective contacts is to replace organic with inorganic contacts (such as replacing SPIRO-OMeTAD with NiO etc.)

Kang Wang *et al* [67] attained remarkable crystallinity and stabilized distorted black phase CsPbI3 thin films by entering hydroiodic acid (HI) and phenylethyl ammonium iodine (PEAI) additives to the CsPbI3 precursor solution. Surprisingly, the PCE of the CsPbI3 perovskite solar cell (PSC) was unexpectedly increased to 15.07%, setting a new record as the highest efficiency yet achieved for an inorganic perovskite cell of this nature. Additionally, the device showed remarkable stability against environmental issues, including humidity, oxygen, and temperature.

Guiata et al [68] switched lead with Sn in MAPbI3 to study the film nucleation growth and stability of MASnI3 perovskite, aiming to incorporate it as the absorber layer in perovskite solar cells (PSCs). This was done to overcome issues associated with lead toxicity. However, Tin based perovskites are more susceptible to quick degradation when compared to Pb-based perovskites. This is due to the corrosion of Sn^{+2} to Sn^{+4}.

Grätzel et al [69] utilized a vacuum flash solution processing technique to make mesostructured TiO2/perovskite solar cells, achieving an impressive PCE of 19.6%. Furthermore, they attained glossy, smooth, and crystalline perovskite films through this method. In order to quickly remove solvent and encourage crystallization of the film during spin coating, Park used diethyl ether as an antisolvent, resulting in an effective TiO_2/perovskite solar cell. Ethyl acetate was testified to produce a compact and pinhole free film as an antisolvent. The quality of the MAPbI3 film could be further improved through the Ostwald recrystallization process while improving the thermal treatment. A MAPbI3 perovskite solar cell with a record high conversion efficiency, incredible reproducibility, and remarkable stability was accomplished while increasing the annealing temperature from 100 to 130°C. The stated highest efficiency stands at approximately 20.3%, and even after 600 hours of storage in room air without encapsulation, the device maintains an impressive 94% of its initial efficiency. Jung *et al* [70] reported Cu doped NiO_2 as HTL through solving process for perovskite solar cells. Cu improved crystallinity and conductivity, which led to a 17.8% rise in PCE.

Chapter 3

Materials and Methods

3.1 Experimental Section

Here, I will discuss the details about experimental parameters for perovskite deposition on top of plane glass substrates and their characterization using different analytical techniques. An appropriate thin-film deposition process was to be selected based on ease of fabrication, availability of in-house resources and reproducibility factor. Thus, spin-coating technique was selected, which is the most used approach towards perovskite deposition. However, the fabrication protocol was restricted to one-step deposition (involving anti-solvent approach) which will be discussed in detail in this chapter.

3.1.1 Chemicals and reagents

Lead (II) Iodide (PbI_2) greater than 99% was procured from Sigma Aldrich (as a main precursor for $MAPbI_3$). Non-anhydrous Dimethylformamide (DMF) was selected as solvent for the ultimate precursor solution. Anhydrous DMF is used for this purpose, however we used non-anhydrous solvent to reduce fabrication cost. Two different non-anhydrous chemicals (i.e, Chlorobenzene and Toluene) were separately studied as anti-solvents in this thesis. Again, a hydrous option was selected to reduce the cost of film deposition. DMF, Chlorobenzene, (CB) and Toluene were purchased from Sigma Aldrich. Methylammonium iodide (MAI) to be added into precursor solution was purchased from Great Cell Solar.

3.1.2 Preparation of glass substrate

Plane glass substrates (i.e., microscope slides) were cleaned by washing them with detergent, followed by sonication for 10 min in deionized water, ethanol, and acetone baths. The substrates were then dried in vacuum (oven) to remove any residual solvents. The surface of glass substrates was chemically activated using concentrated HCl

solution. The substrates were then spin-coated using MAPbI$_3$ precursor solution by following the protocol explained in the subsequent text.

3.1.3 Preparation of MAPbI3 precursor solution

The precursor solution was prepared by keeping the PbI$_2$ concentration as 1M. Since one-step approach was used in this study, the molar ratio of 1:1 was maintained between PbI$_2$ and MAI (CH$_3$NH$_3$I) to prepare the final solution. Similar molar ratios have been repeatedly used in the previously reported research works [71, 72]. These two precursors were then dissolved in dimethylformamide (DMF) while stirring at 120 °C for at least 20 min. Higher temperature was maintained during stirring to ensure complete dissolution and homogenization of the PbI$_2$ and MAI in the DMF solvent before initiating the film deposition process. Process
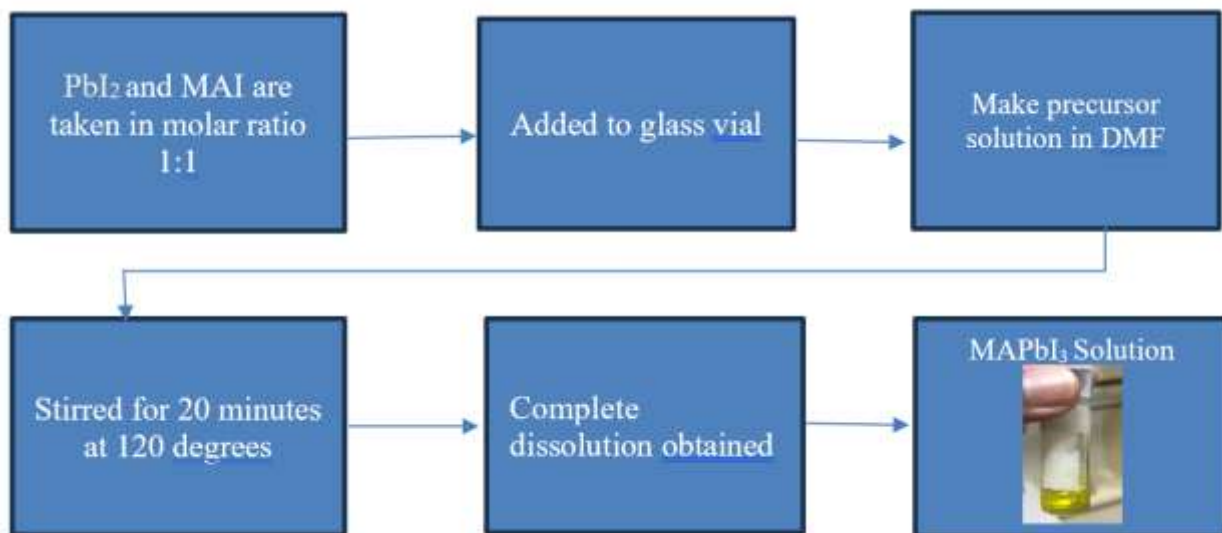
Figure 3. 1. Synthesis of MAPbI3 precursor solution

3.1.4 spin coating and antisolvent application

Chemically activated glass substrates were securely placed on the chuck of the spin-coating setup. To create the perovskite film, 100 μl of the MAPbI$_3$ precursor solution was carefully dropped on top the glass substrate using a micropipette or syringe. This

was done before starting the spin program. The spin coating was then performed at 3000rpm for about 30 seconds. The spin-coating process is initiated with special attention to maintaining a smooth and consistent acceleration and deceleration profile. As the spinning process progresses, the precursor solution spreads out on the substrate, resulting in the formation of a thin film. 50 µl of antisolvent (i.e., the chlorobenzene and/or toluene) were rapidly dropped on top of the spinning substrate. The anti-solvents were dropped at different time intervals to investigate the differences in film quality and morphology. The time for dropping the anti-solvents were selected to be: (1). during startup (or just when the spin program is started) (2). 15 sec before the spin program stops and (3). 5 sec before the spin program stops. The introduction of the antisolvent triggers rapid crystallization of the perovskite material, contributing to the development of a uniform and compact film structure.
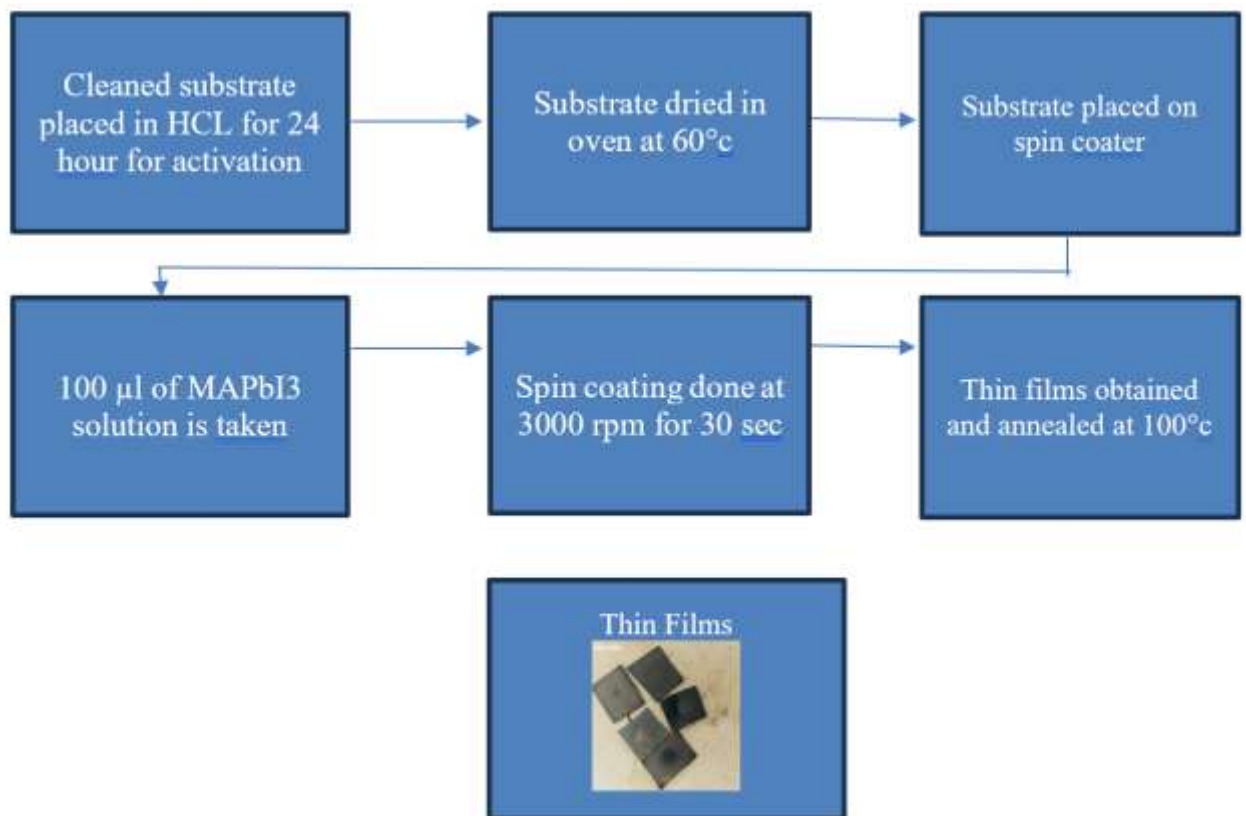
Figure 3. 2. Spin coating of MAPbI3 on glass substrate

Figure 3. 3. Spin coating setup for making thin films.

3.1.5 Thermal Annealing

Immediately after spin-coating, the MAPbI$_3$ coated glass substrates were transferred placed on the hot plate at 100 ^{o}C for 10 to 20 min (under ambient conditions). It is important to be noted here that all the perovskite deposition and annealing processes were performed under ambient conditions instead of commonly used inert environment[73]. The purpose of this annealing step is twofold. First, to eliminate any residual solvents present in the film. Secondly, the annealing process promotes the reaction between MAI and PbI$_2$ to form well-structured and crystalline MAPbI$_3$ perovskite film. By subjecting the coated substrate to controlled thermal conditions, the film undergoes further transformations, resulting in improved film quality and the enhancement of desired perovskite crystal properties. This annealing step is crucial for achieving the desired material characteristics, making the substrate ready for subsequent applications in various optoelectronic and photovoltaic devices.

3.1.6. Characterization

Following the annealing process, the substrate is allowed to cool down at room temperature naturally. During this cooling phase, the MAPbI3 perovskite film undergoes further stabilization, ensuring its structural integrity and proper crystallization.

To thoroughly analyze and characterize the resulting perovskite film, a range of techniques can be employed. XRD allows for the examination of the film's crystal

structure and phase purity, providing insights into its long-range ordering. Scanning electron microscopy (SEM) enables high-resolution imaging of the film's surface morphology and microstructure, revealing its topographical features and grain sizes.

UV-Vis is utilized to study the film's optical properties and absorbance spectra, providing information about its bandgap and light absorption characteristics. Hall-Effect measurements help determine the film's electrical conductivity, carrier concentration, and mobility, offering valuable data on its electronic properties.

Finally, FTIR aids in identifying functional groups and chemical bonds in the perovskite film, further validating its composition and structure. Through the comprehensive analysis of these various techniques, a comprehensive understanding of the MAPbI3 perovskite film's properties can be obtained, essential for evaluating its suitability and performance in specific applications such as photovoltaic devices or other optoelectronic technologies.

Chapter 4

Characterization Techniques

Characteristics of synthesized methyl ammonium lead iodide based perovskite thin films were investigated through specific analysis techniques. This chapter will give a short review of all techniques used to examine MAPbI3 based thin films. Following are the characterization techniques followed:

4.1. X ray diffraction

It is a characterization technique mainly used for phase studies and unit cell information for crystalline materials. Firstly, it Max Von Laue was discovered it in 1912, additional he discovered that crystals act as 3D materials and their lattice planes acts as grating for x-ray. The wavelength of X-rays is ranging from 10^oA to 8 nm, but the wavelength applied for consideration is from 10^oA to 2.5 nm. Sample for analysis should be crystalline in nature, crystallite powder and flat surfaces be appropriate to organic, inorganic, polymers, metals, and different composites [74].

X ray generation

It usually consists of electron source finalized in a tube, heated tungsten element is used as electron gun and electrons from it shine on a metal target, metal target is typically water-cooled Cu metal. When electron beam relates with metal target atoms it causes inner orbital electron frees that happened due to high energy electrons and metal atoms interaction. When this removed excited electron deexcited and set back to ground state then it will emit energy in photons of higher energy those high energy emitted photons are called X-rays. That radiated X-rays are a function of metal target. So, each metal has its own characteristics X-rays. Copper target commonly produces two characteristic X-Rays called Cu Kα (λ = 0.154 nm) and Cu Kβ (λ=0.139 nm) widely used in X-ray diffractometers in world. [74]

Material Studying

X-rays are generated in an X-ray tube and then directed through a beryllium window and slits. These X-rays are then directed onto the material of interest. When the X-rays interact with the crystal lattice planes of the substance, they are diffracted back at

specific angles. The diffracted X-ray beam is then identified and measured using a solid scintillation counter, which can rotate to different angles.

The material's fascinating response to the incident X-rays is recorded as a diffractogram. In the diffractogram, different peaks with varying intensities appear at individual diffraction angles. These peaks and their intensities hold necessary information about the material's crystalline properties. Particularly, they provide understandings into the crystallite size, space group, interplanar spacing, and long-range lattice order of the material.

Each crystalline material has its identifiable diffractogram, making X-ray diffraction a powerful technique for identifying and characterizing different materials based on their crystal structures and properties. By analyzing the diffractogram, researchers can gain significant knowledge about the arrangement of atoms in the material, which is fundamental for various scientific and technological applications. [75]

Calculations

Bragg's law is heart of diffractogram calculations, which is defined as:

$$Sin\ \theta = n\lambda/2d$$

Where, θ represents angle of incidence, n is a whole number, and d is the interplanar distance and λ is wavelength of incident x-ray.
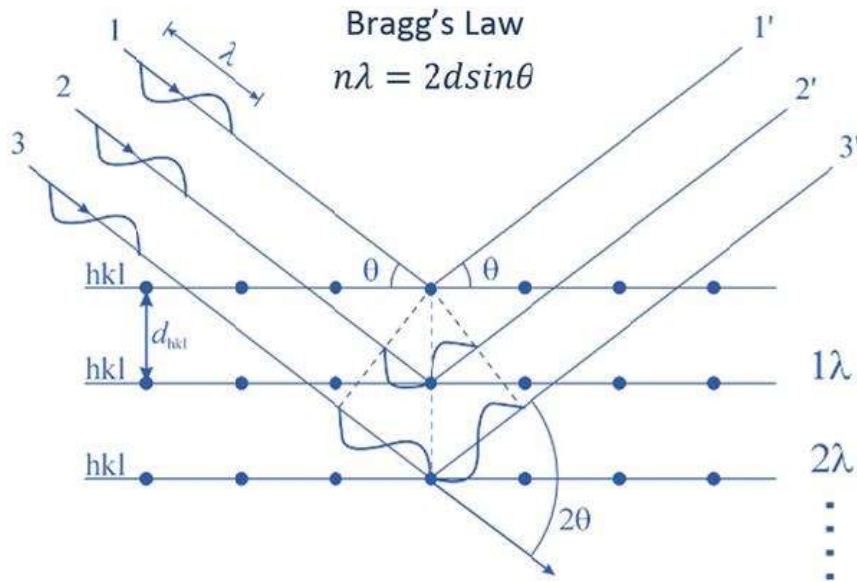
Figure 4. 1. X-Ray Scattering

For calculation of crystallite size Debye's Scherer formula is used. The equation is given below.

$$D=K\lambda/\beta\cos\theta$$

Here wavelength is λ, β is FWHM, θ represents diffraction angle and K is Scherrer's constant. Also, x-ray gives the aggregate data of crystallite sizes and in most cases, it does not follows standard patterns for a sizeable measure of powder.

X ray diffractometer that is being used in our research is STOE Stadi MP which is using Cu Kα ($\lambda = 0.154$ nm) source in θ-2θ. [76]

4.2. Scanning Electron microscopy

Scanning electron microscopy is a important method used to inspect and analyze various aspects of sample materials, such as their morphology, microstructure, size, shape, phase differences, and surface topography.

In SEM, an electron beam produced by a heated filament source (electron gun) is

targeted and focused on surface of the sample using objective and condenser lenses. The focused electron beam then interacts with the sample, resulting in elastic or inelastic scattering processes.

By using SEM, researchers can gain precious insights into the properties and characteristics of materials at a microscopic level. This technique permits the imagining and examination of surface features, internal structures, and chemical composition, making it an indispensable tool in various scientific and industrial applications [77].
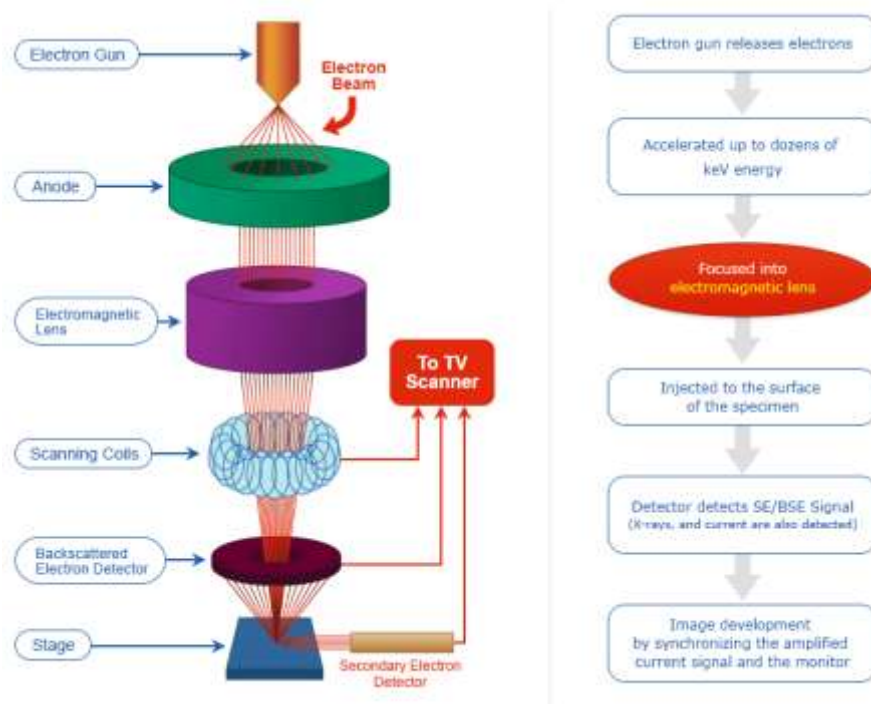
Figure 4. 2. Schematic diagram of scanning electron microscopy

The interaction between the electron beam and the sample in scanning electron microscopy (SEM) delivers valuable insights into the sample's characteristics, including morphology, external structure, chemical composition, and crystalline structure. The elastic interaction reveals compositional differences, while the inelastic interaction generates secondary electrons that show surface information. Our analysis of numerous samples was performed using the JEOL JSM-64900 SEM model, which allows us to

investigate and characterize materials at a micro- and nanoscale level [78].

4.3. Ultraviolet visible spectroscopy (UV-vis)

Introduction

UV-Vis spectroscopy is an absorption spectroscopy procedure, molecules absorb radiation in the range of 200 to1000nm and this absorption leads to electrons transition in the molecules. Specified electron transitions shown certain energy absorbance so UV-Vis plot will offer photon energy absorbance characteristics of sample [79].

Working principle

Its working is opposite to the emission spectroscopy, because in emission spectroscopy photons emitted because of electron transition from higher to lower energy levels while in UV-Vis spectroscopy certain energy photon absorbance will occurred due to electronic transition from lower to higher energy levels.

As electronic transition due to absorbance of photons is determined in UV-Vis spectroscopy so it will also be called as electronic spectroscopy [80].

Calculations

The theory on which UV Vis spectroscopy is being performed is Beer lambert's law. Beer lambert's law states that when monochromatic light travel some material it will absorb some light that results in reduction to intensity of light that will function of path length from solution and concentration of solution. The mathematical form of Beer Lambert Law is as following:

$$A = \log \frac{Io}{I} = \mathcal{E}cL$$

Where, A ,I_0 and I are absorbance, incident light intensity and intensity of light later absorption respectively, while c is molar concentration of solution in mol/dm^3, and L is path length typically its breadth of sample cell (cm) while $\mathcal{E}$ is molar absorptivity of material. [81]

Electron excitation in molecules

The absorption of radiation in the UV and visible region primarily influences the electronic state of molecules. When the energy of whole electrons in a molecule is at a

minimum, it is in its ground state. Upon exposure to radiation, the molecules absorb energy, causing electrons to transition to higher energy levels, called the excited state.

This process of electrons moving to higher energy levels is referred to as electronic excitation. The UV-visible region of the electromagnetic spectrum is remarkably effective at inducing electronic excitation in molecules. The frequency of a photon (ν) in the radiation is directly related to its energy (ΔE) through the equation $\Delta E = h\nu$, where h is Planck's constant [82].

The specific amount of energy required for electronic excitation depends exactly on the energy difference between the ground state energy (E_o) and the excited state energy (E') of the electrons.

.The relationship is described as following:

$$\Delta E = E' - E^o = h\upsilon$$

In many molecules, electrons are normally found in nonbonding or bonding π orbitals. When these electrons absorb a photon of energy, they transition to advanced energy unoccupied molecular orbitals, which can be either anti-bonding π* or σ* orbitals. The molecular orbitals are commonly displayed in the order of σ, π, π*, and σ* from lower to higher energy, with σ bonds having the lowest energy and σ* orbitals having the highest energy.

Depending on the identifiable bonds and functional groups present in a molecule, various electron transitions become possible, such as π-σ and π-π transitions. Each of these transitions includes the absorption of quantized radiation with a particular amount of energy.

In summary, molecules display different electronic transitions due to the presence of various molecular orbitals and bonding configurations, and each transition requires the absorption of specific quantized radiation energy.
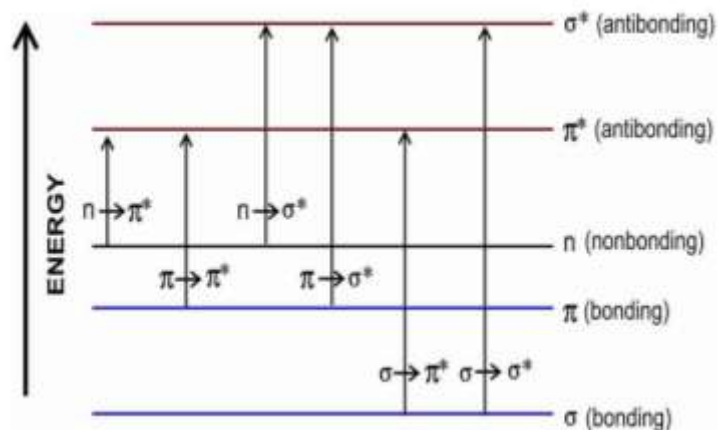
Figure 4. 3. Electronic transitions in UV-vis spectroscopy[83]

Working

UV-Visible spectrometer is either a single beam or double beam instruments. Firstly, in a single beam intensity of reference (solvent or air) is measured and then the intensity of the sample is measured. In double-beam instrument, simultaneous recording of radiation beam intensity from reference and sample is recorded.

Monochromatic light is fallen on sample and change in light intensity is measured by detectors then plot is recorded and displayed.
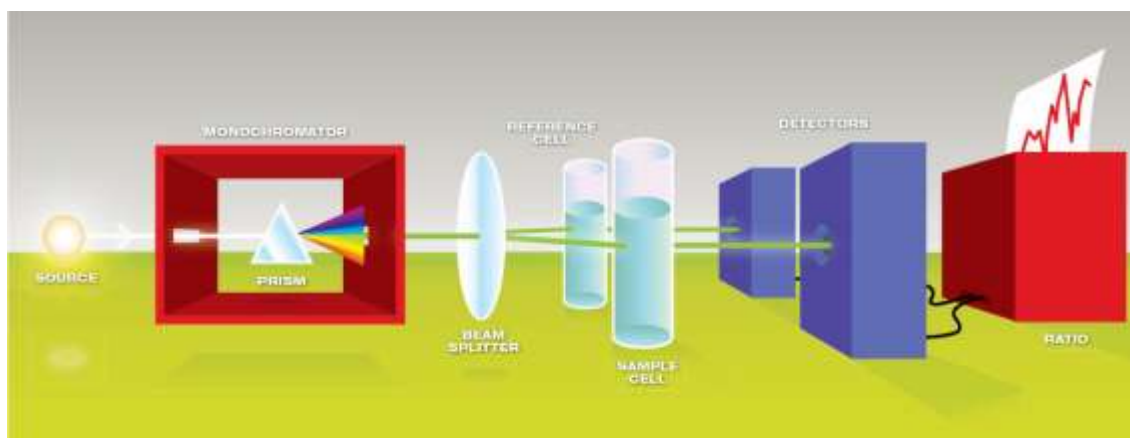
Figure 4. 4. Double beam UV-vis spectrometer schematic

Qualitative information

The qualitative information is attained by seeing the UV/Vis spectrum which is the absorption of UV visible radiation versus wavelength. The spectrum may be drawn as wavelength versus transmittance or Ɛ (molar absorptivity)

Quantitative information

This can also be acquired by taking the readings of absorption or emission of UV visible radiations by molecules or ions using a Beer-Lambert law. Spectrums obtained can be used to calculate the band gap of material via using Tauc plot equation.

$$\mathcal{E}h\upsilon = (h\upsilon - Eg)^n$$

Where Ɛ = Absorption, h = Planks constant, υ = frequency, Eg= band gap, n= ½ for direct and 2 for indirect bandgap.

During these research JENWAY 7315 UV-vis spectrometers was used having single beam configuration with xenon lamp and monochromator. 10 mm path length quartz cuvette is used for sample holding. [84]

Figure 4. 5. JENWAY 7315 UV-vis spectrometer

4.4. Hall effect measurements

Introduction

In 1879, Edwin Hall discovered the Hall effect, which has since become a valuable technique for measuring electrical properties of thin films. It operates based on the principles of electromagnetism. The Hall effect apparatus allows for the determination of various electrical parameters of thin films, such as sheet resistance, bulk carrier concentration, and DC-Hall effect measurements. By using this method, researchers can measure resistivity, conductivity, sheet resistance, and sheet carrier mobility of the thin films accurately. [85]

Working principle

When a moving charge is subjected to a magnetic field, it experiences the Lorentz force. This force leads to the generation of potential across the conductor. As a result, positive charges accumulate on one end of the conductor, while negative charges accumulate on the opposite end. This charge buildup creates an outward force perpendicular to the plane of the conductor, known as the Lorentz force. The potential developed across the conductor due to this charge accumulation is referred to as the Hall Voltage.

Lorentz force is given by below equation:

$$F = e(\upsilon \times B)[86]$$

Where, B is magnetic field along z axis, e is charge on electron and υ is velocity of charge carrier.
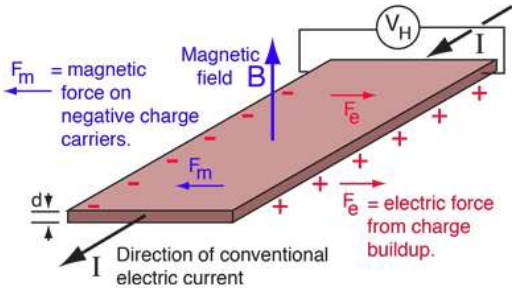
Figure 4. 6. Hall effect working principle[87]

4.5. Fourier transformation infrared spectroscopy (FTIR)

Fourier Transform Infrared Spectroscopy (FTIR) is a valuable analytical method utilized to identify and quantify unknown organic and polymeric substances. It is primarily employed for qualitative analysis purposes [88].
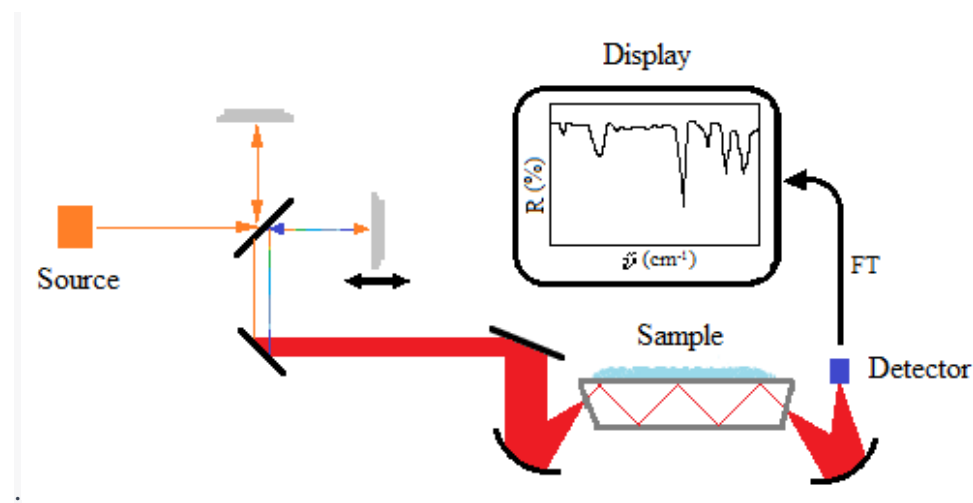
Figure 4. 7. Instrument schematic[89]

The FTIR instrument utilizes infrared (IR) radiation in the range of approximately 10,000 to 100 cm^-1, typically from 4000 cm^-1 to 400 cm^-1. When this radiation interacts with a material, some of it gets absorbed, and the rest passes through. The absorbed radiation imparts rotational or vibrational energy to the molecules of the material. The changes in the IR spectra caused by these interactions are recorded by a detector. Each type of molecule produces a unique spectral fingerprint, which serves as a distinctive identifier for molecular matching and identification. By analyzing the absorption bands and characteristic fingerprints, FTIR can effectively detect changes in the composition or impurities present in the material. As a result, FTIR proves to be a powerful and reliable tool for the identification of molecules and the qualitative analysis of substances [90].

.
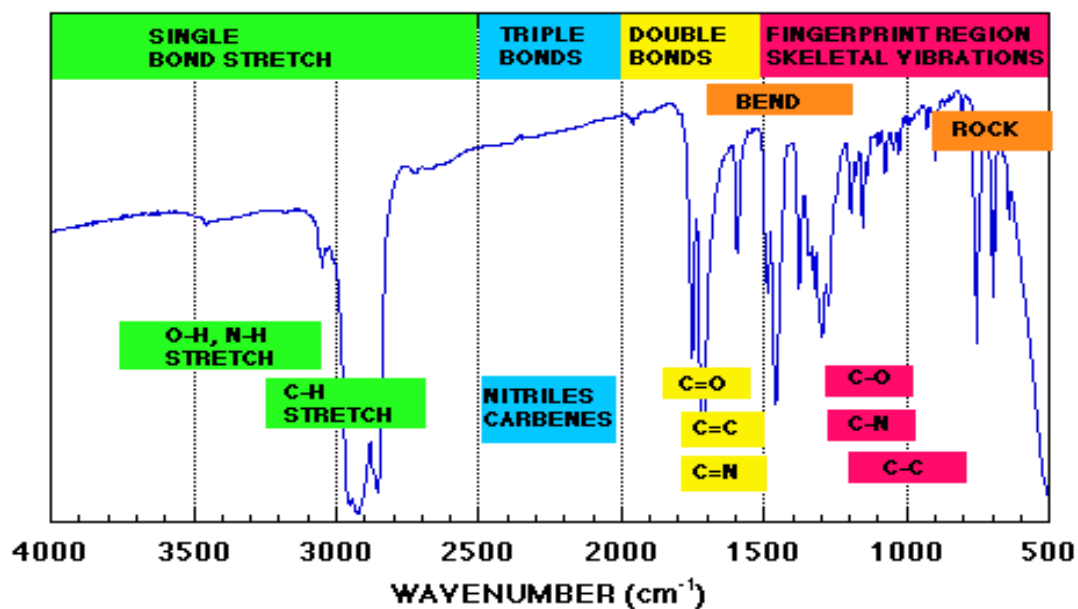
Figure 4. 8. Standard FTIR Spectra with fingerprint regions[91]

When standard reference sample is available and chemistry is well known then FTIR can be used to quantify specific functional group as quantitative tool, in this roll intensity of absorbance wave will quantify the quantity of functional group in material.

In this research work, Agilent Cary 630 FTIR was used to identify the organic surfactant present on surface of the perovskite films.

Figure 4. 9. Agilent Cary 630 FTIR [92]

Chapter 5

Results and discussions

5.1. The nomenclature used for the samples:

I started with studying the crystal structure of the MAPbI$_3$ thin films (on top of glass substrates). For this, I carried out ***X-ray diffraction (XRD)*** measurements. To investigate the effect of anti-solvents and the time (of its application on top of spinning substrate), on film morphology and surface coverage, I carried out ***SEM*** measurements. The absorption studies, electrical properties and the confirmation of chemical bonds were further studied using ***UV-Vis***, ***Hall-effect*** and ***FTIR*** respectively. The results from all these measurements are discussed in detail in this chapter. The nomenclature for the samples used in this research work is listed as follows:

(a). **Control:** The MAPbI$_3$ samples prepared ***without*** using any anti-solvent. These samples were used as reference for general comparison.

(b). **CB-5:** The MAPbI$_3$ samples prepared by dropping the ***Chlorobenzene*** anti-solvent at ***5 sec*** before the spin-program stopped.

(c). **TL-5:** The MAPbI$_3$ samples prepared by dropping the ***Toluene*** anti-solvent at ***5 sec*** before the spin-program stopped.

(b). **CB-15*:*** The MAPbI$_3$ samples prepared by dropping the ***Chlorobenzene*** anti-solvent at ***15 sec*** before the spin-program stopped.

(c). **TL-15:** The MAPbI$_3$ samples prepared by dropping the ***Toluene*** anti-solvent at ***15 sec*** before the spin-program stopped.

(f). **CB-St:** The MAPbI$_3$ samples prepared by dropping the ***Chlorobenzene*** anti-solvent within ***first 5 sec*** of the spin-program.

(g). **TL-St:** The MAPbI$_3$ samples prepared by dropping the ***Toluene*** anti-solvent within ***first 5 sec*** of the spin-program.

5.1.2 X-Ray Diffraction (XRD)

Figures 5.1 presents the X-ray diffraction (XRD) patterns of CH$_3$NH$_3$PbI$_3$ perovskite

films, obtained by varying the dripping time of two different antisolvents (toluene and chlorobenzene). It shows Bragg reflection peaks at 12.5° and 14.0° which corresponds to the planes of miller indices (h k l) as (001) and (110) respectively. The observed diffraction peaks at 12.5°and 14.0° closely match to **JCPDS-96-451-8044** depicting the formation of MAPbI3 based perovskite films.[93]

From fig 5.2 it is observed the crystallite size vary as we change the dripping time of antisolvent. values for average crystal size are given in Table. Moreover, peak for unreacted lead iodide is also diminished in some cases. For **CB-5** and **Tol-5** peak corresponds to lead iodide totally disappeared. For **CB-15** and **Tol-15** peak corresponds to unreacted lead iodide is quite diminishes as compared to the pattern observed for **CB-St** and **Tol- St.**
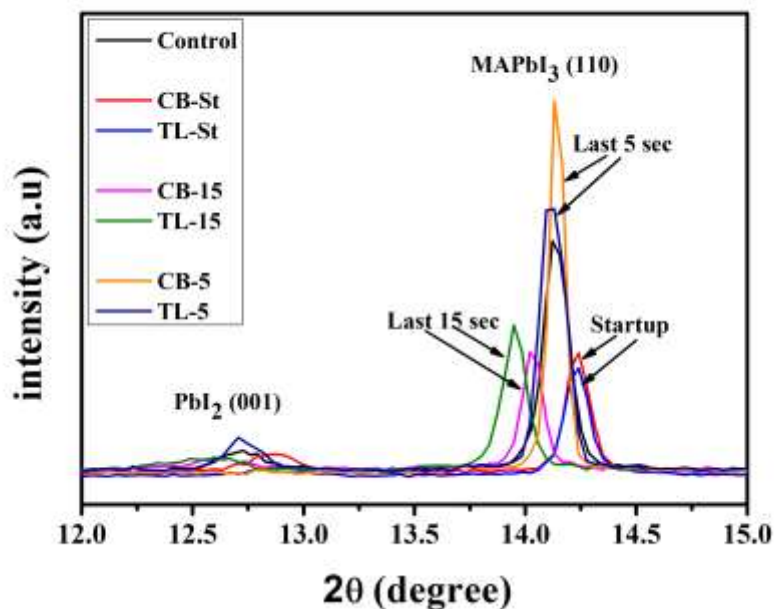
Figure 5. 1. Combined XRD of MAPbI₃ for comparison
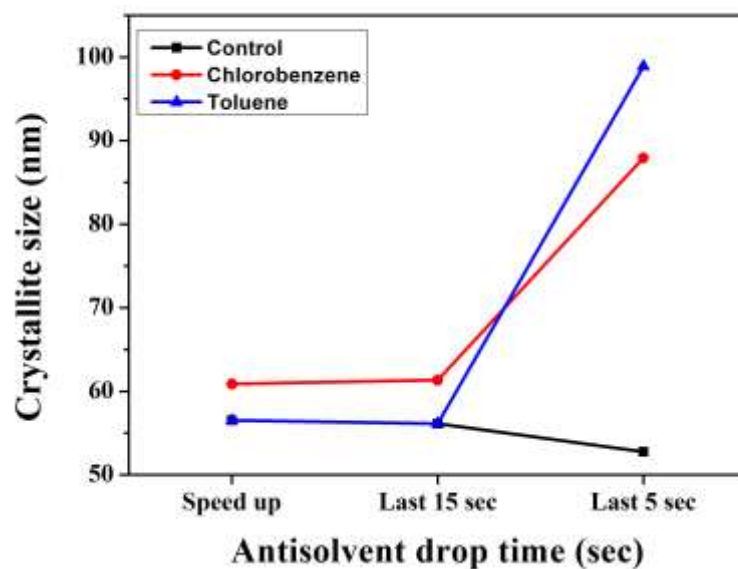
Figure 5. 2. Combined graph of crystallite size for comparison

Table 1. Crystallite size (in nm) as a function of anti-solvent drop time (in sec)

AS Drop time	Crystallite size (nm)		
	Control	Chlorobenzene	Toluene
Speed up	56.53	60.88	56.54
Last 15 sec	56.12	61.34	56.12
Last 5 sec	52.76	87.93	98.92

5.2 Scanning Electron Microscopy (SEM)

SEM micrographs of MAPbI3 shows uniform morphology when antisolvents such as chlorobenzene and toluene are added right after the spinning process begins (**CB-St and Tol- St**). The rapid addition of antisolvent leads to fast crystallization, resulting in a smooth film structure. For **controlled** MAPbI$_3$ films it shows flake-like structure, which is attributed to higher humidity conditions, allowing the crystals more time to grow. Upon closer examination, the overall study indicates that the addition of antisolvents just a few seconds after the spinning process starts yields significant results. The resulting perovskite film displays improved morphology with fewer pinholes, highlighting the effectiveness of this technique in achieving a desired film structure for potential applications in optoelectronic devices.
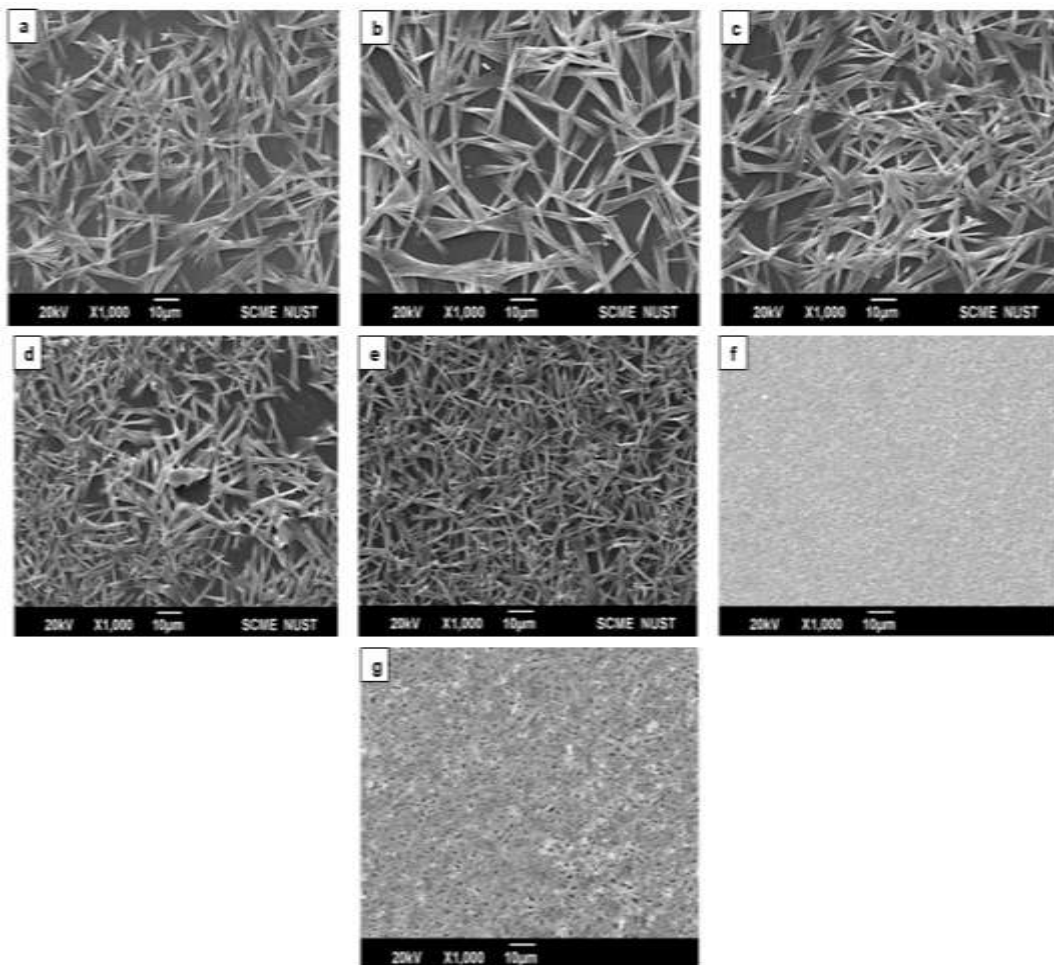
Figure 5. 3. Control (b). CB at last 5 sec (c) Toluene at last 5 sec (d) Chlorobenzene at 15 seconds (e). Toluene at 15 sec (f). Chlorobenzene at startup (g). Toluene at startup

43

5.3. UV-Vis Spectroscopy

Figure 4 shows absorbance spectra of MAPbI$_3$ perovskite absorbers layer with and without antisolvent. Results revealed that the perovskite film treated with antisolvent immediately after the spin programme started (**TOL-St** and **CB-St)** exhibits a prominent absorption peak around 750 nm which closely match to literature reported value for formation of methyl ammonium lead iodide.[94]

Additionally in Figures 5 and 6 the measured bandgap values for MAPbI$_3$ absorber layer are presented, particularly for films treated with antisolvents (chlorobenzene and toluene) treatment immediately after the spinning process started (**TOL-St** and **CB-St)**. The optical bandgap of the films was estimated from the absorbance data using the expression:

$$\alpha h\nu = A(h\nu - Eg)^n$$

Here, h represents Planck's constant, ν is the frequency of incident UV-Vis radiations, A represents constant, α is the absorption coefficient in cm^{-1}, hν is the photon energy in eV, and n takes a value of ½ for direct band gap semiconductors and 2 for indirect band gap semiconductors.

The calculated band gap values for MAPbI$_3$ films treated with antisolvents at speed up (**TOL-St** and **CB-St)** were found to be 1.4 eV and 1.43 eV. These calculated band gap values closely match the literature-reported values [94].
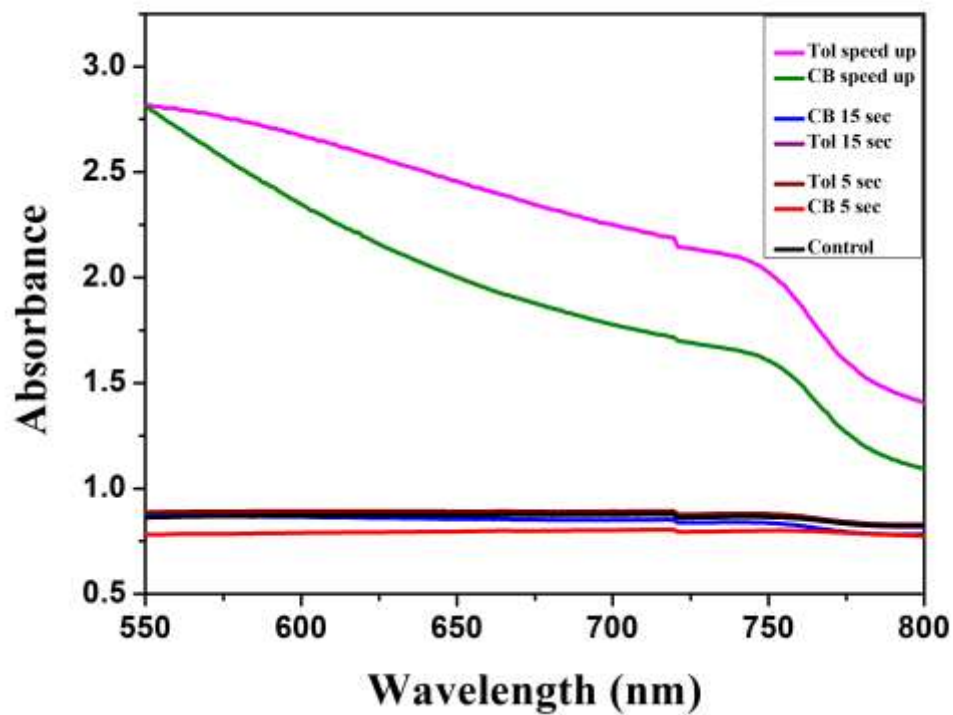
Figure 5. 4. UV-Vis results of absorption spectra for MAPbI3 based thin films
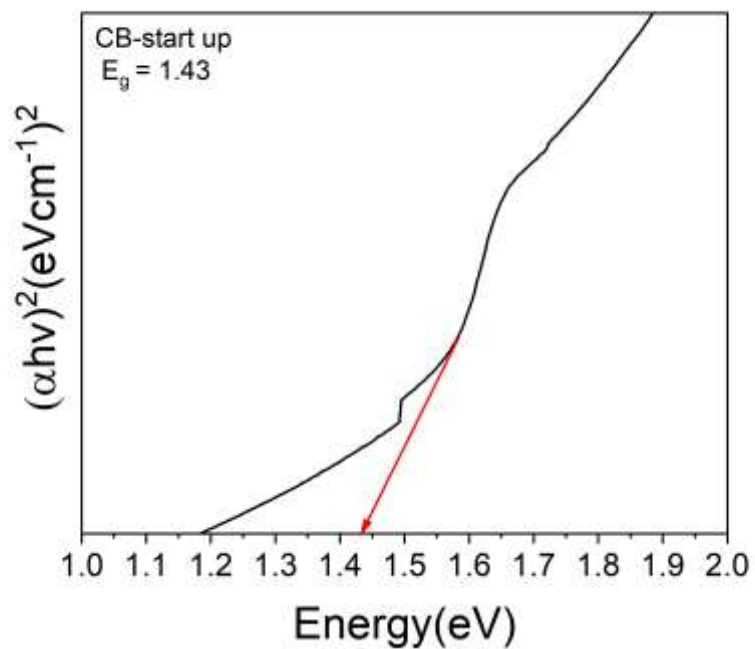
Figure 5. 5. Band Gap Plot: MAPbI3 Films with CB at start up of spinning programme
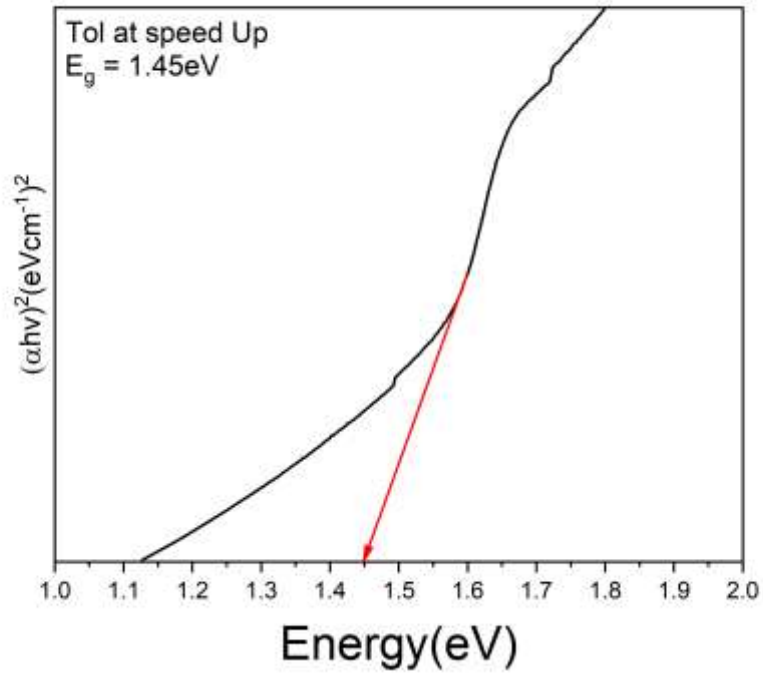
Figure 5. 6. Band Gap Plot: MAPbI$_3$ Films with Toluene Antisolvent After Spinning Initiation

5.4. Hall Effect Measurements

Hall effect confirms the conductivity type of semiconductors. In our study, we performed Hall effect measurements on MAPbI$_3$ based perovskite films with and without addition of different antisolvent by varying drop of time. Hall effect measurements are shown in table 2. The results showed that films synthesized without antisolvent have positive values for Hall coefficient and bulk concentration, so conductivity type is P-type. This result match with literature reported value.[95]

However, when we introduced antisolvent (chlorobenzene) during the spinning process**(CB -St)**, the mobility of the film increased significantly. Interestingly, the Hall coefficient and bulk concentration changed from positive to negative value, representing a switch in conductivity type from P-type to N-type. Moreover, when chlorobenzene antisolvent was added at half time of the spinning process **(CB-15),** the values for Hall coefficient and carrier concentration are still negative, indicating N-type conductivity.

However, the mobility was notably higher than in the previous case**(CB-15)**. Additionally, by introducing chlorobenzene antisolvent for the last five seconds of the spinning process**(CB-5)**, the Hall coefficient and bulk concentration changed to positive values, which shows that conductivity is P-type. Nevertheless, a rapid change in mobility was observed in this case.

Furthermore, when antisolvent toluene was added just after the spinning process began **(Tol-St)**, the conductivity type remained P-type. When antisolvent is added five seconds before the end of the process**(Tol-5)** the conductivity type will remain P-type but value for mobility decreases. When toluene was added at the midway point of the spinning process **(Tol-15)**, the conductivity type switched to N-type, with negative values for the Hall coefficient and bulk concentration.

These outcomes highlight the significant effect of antisolvent addition on the conductivity type and mobility of MAPbI$_3$ perovskite absorber layer. Realizing these effects can be important for optimizing the electrical properties of such PV applications.

Table 2. The results for Resistivity, conductivity, mobility. Hall co-efficient and bulk concentration.

Sample name	Hall Coefficient R_H (cm^3/c)	Electrical conductivity σ (1/Ωcm)	Resistivity (Ω cm)	Electron mobility, μ_e (cm^2/vs)	Bulk concentration (1/cm^3)
without antisolvent	5.162 x 10^5	5.670 x 10^{-7}	1.764 x 10^6	2.927x 10^{-1}	1.209 x 10^{13}
MAPbI3 (CB at speed up)	-2.142 x 10^5	6.628 x 10^{-5}	1.509x10^4	9.17 x 10^0	-1.354 x 10^9
Chlorobenzene At 15	-5.0961 x 10^6	5.105 x 10^{-5}	1.959 x 10^4	3.043 x 10^2	-1.047 x 10^8
Chlorobenzene At 5	1.001 x 10^5	1.713 x 10^{-5}	5.837 x 10^4	1.75 x 10^0	6.235 x 10^9
Toluene at speedup	1.552 x 10^5	8.259 x 10^{-5}	1.211 x 10^4	3.478 x 10^2	1.482 x 10^{12}
Toluene at 15	-4.888 x 10^6	2.07 x 10^{-5}	4.830 x 10^4	1.012 x 10^2	-1.277 x 10^8
Toluene at 5	2.682 x 10^6	2.533 x 10^{-5}	3.917 x 10^1	6.84 x 10^1	2.38 x 10^{-5}

5.5. Fourier Transform Infrared Spectroscopy (FTIR)

All the samples were subjected to Fourier Transform IR spectroscopy through a range of 400-4000 cm^{-1}. This was done for the confirmation of functional group in all the samples. The peaks observed were almost similar for all the samples. The methyl functional groups peaks were observed at 906.3 cm^{-1}, and C-H scissoring at 1461.67 cm^{-1}.[96] The N-H bend and C-H bend peaks were observed at 1632.02 cm$^-$

[1] and 1745.56 cm^{-1}.[97] Sharp C-H stretches at 2853.94 cm^{-1} and 2924.05 cm^{-1} were also observed. The OH stretch was significant and prominent in all the samples at 3421.2 cm^{-1}.[98] The N-H peak belongs to perovskite. In contrast, in the peaks observed for toluene-perovskite film, the N–H vibration peaks for MAPbI3 at 1461 cm^{-1} were relatively weak than that of chlorobenzene. [99]
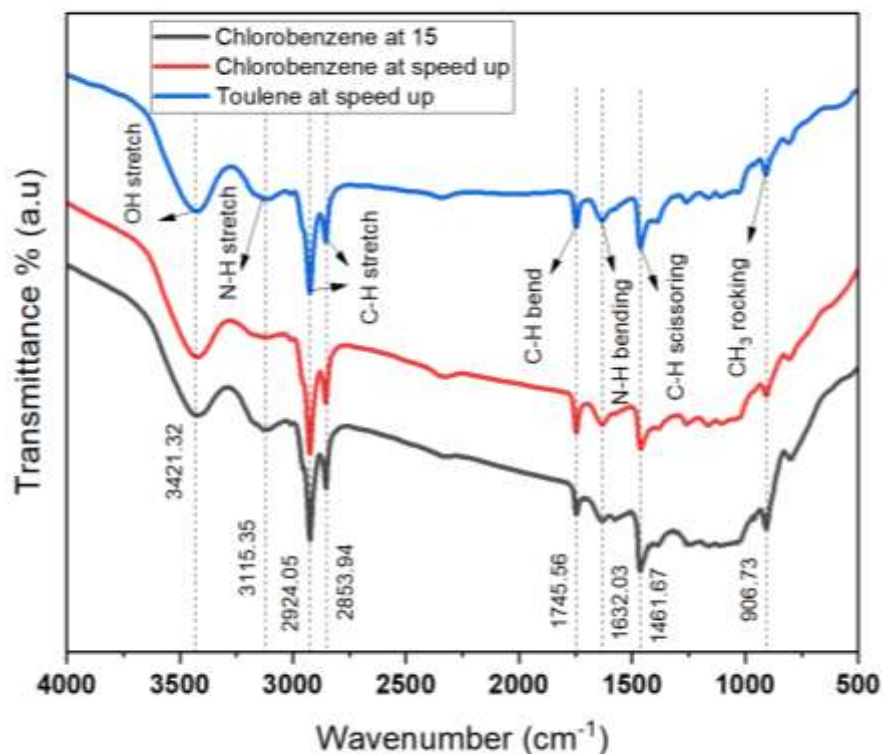
Figure 5. 7. FTIR of MAPBI3 prepared by addition of Toluene. chlorobenzene at speed up and chlorobenzene at 15 (top to bottom)

Conclusion

In this thesis, we successfully synthesized methyl ammonium lead iodide (MAPbI3) based perovskite thin films using a one-step antisolvent method. Our study involved a comparative analysis of two antisolvents(chlorobenzene and toluene) and investigated the influence of their application time on the thin film properties. The X-ray diffraction (XRD) analysis provided conclusive evidence of the formation of MAPbI3 in the thin films, confirming the successful synthesis of the perovskite absorber layer. Complementary to this, scanning electron microscopy (SEM) images showcased significant improvement in the thin film morphology when toluene was introduced at the start of the spinning program. Furthermore, our UV-visible (UV-vis) spectroscopy results revealed fascinating optical properties of perovskite films. Notably, using toluene during the speed-up phase led to better light absorption with band gap of 1.4eV. Moreover, our study delved into the electrical behavior of the MAPbI3 thin films through Hall effect measurements shows that the films synthesized using toluene exhibited higher conductivity, displaying a P-type conduction behavior. FTIR results corroborated the successful synthesis of MAPbI3 and provided valuable insights into the molecular structure of the thin films.

References

[1]   K. S. Ahmad, S. N. Naqvi, and S. B. J. R. i. i. c. Jaffri, "Systematic review elucidating the generations and classifications of solar cells contributing towards environmental sustainability integration," vol. 41, pp. 21-39, (2021).

[2]   A. O. Maka and J. M. J. C. E. Alabid, "Solar energy technology and its roles in sustainable development," vol. 6, pp. 476-483, (2022).

[3]   O. Ellabban, H. Abu-Rub, F. J. R. Blaabjerg, and s. e. reviews, "Renewable energy resources: Current status, future prospects and their enabling technology," vol. 39, pp. 748-764, (2014).

[4]   X. Wang, X. Lu, B. Liu, D. Chen, Y. Tong, and G. J. A. m. Shen, "Flexible energy- storage devices: design consideration and recent progress," vol. 26, pp. 4763-4782, (2014).

[5]   A. M. Bagher, M. M. A. Vahid, M. J. A. J. o. o. Mohsen, and Photonics, "Types of solar cells and application," vol. 3, pp. 94-113, (2015).

[6]   R. King, D. Bhusari, D. Larrabee, X. Q. Liu, E. Rehder, K. Edmondson, *et al.*, "Solar cell generations over 40% efficiency," vol. 20, pp. 801-815, (2012).

[7]   A. Khatibi, F. Razi Astaraei, M. H. J. E. S. Ahmadi, and Engineering, "Generation and combination of the solar cells: A current model review," vol. 7, pp. 305-322, (2019).

[8]   O. Vigil-Galán, M. Courel, J. Andrade-Arvizu, Y. Sánchez, M. Espíndola-Rodríguez, E. Saucedo, *et al.*, "Route towards low cost-high efficiency second generation solar cells: current status and perspectives," vol. 26, pp. 5562-5573, (2015).

[9]   M. M. A. Moon, M. F. Rahman, J. Hossain, and A. B. M. J. A. M. R. Ismail, "Comparative study of the second generation a-Si: H, CdTe, and CIGS thin-film solar cells," vol. 1154, pp. 102-111, (2019).

[10]   G. J. M. t. Conibeer, "Third-generation photovoltaics," vol. 10, pp. 42-50, 2007.

[11]   M. A. Green, A. Ho-Baillie, and H. J. J. N. p. Snaith, "The emergence of perovskite solar cells," vol. 8, pp. 506-514, (2014).

[12]   Z. Tang, Z. George, Z. Ma, J. Bergqvist, K. Tvingstedt, K. Vandewal, *et al.*,

"Semi- transparent tandem organic solar cells with 90% Internal Quantum Efficiency," vol. 2, pp. 1467-1476, (2012).

[13]   J.-H. Kim and S.-H. J. S. Han, "Energy generation performance of window-type dye-sensitized solar cells by color and transmittance," vol. 12, p. 8961, (2020).

[14]   J. You, Y. M. Yang, Z. Hong, T.-B. Song, L. Meng, Y. Liu*, et al.*, "Moisture assisted perovskite film growth for high performance solar cells," vol. 105, (2014).

[15]   Z. Huang, D. Wang, S. Wang, and T. J. M. Zhang, "Highly efficient and stable MAPbI3 perovskite solar cell induced by regulated nucleation and Ostwald recrystallization," vol. 11, p. 778, (2018).

[16]   M. Saliba, J. P. Correa- Baena, M. Grätzel, A. Hagfeldt, and A. J. A. C. I. E. Abate, "Perovskite solar cells: from the atomic level to film quality and device performance," vol. 57, pp. 2554-2569, (2018).

[17]   R. K. Misra, S. Aharon, M. Layani, S. Magdassi, and L. J. J. o. M. C. A. Etgar, "A mesoporous–planar hybrid architecture of methylammonium lead iodide perovskite based solar cells," vol. 4, pp. 14423-14429, (2016).

[18]   Y.-F. Chen, Y.-T. Tsai, D. Bassani, R. Clerc, D. Forgács, H. Bolink*, et al.*, "Evidence of band bending induced by hole trapping at MAPbI 3 perovskite/metal interface," vol. 4, pp. 17529-17536, (2016).

[19]   N. Baig, I. Kammakakam, and W. J. M. A. Falath, "Nanomaterials: A review of synthesis methods, properties, recent progress, and challenges," vol. 2, pp. 1821-1871, (2021).

[20]   H. Sung, N. Ahn, M. S. Jang, J. K. Lee, H. Yoon, N. G. Park*, et al.*, "Transparent conductive oxide- free graphene- based perovskite solar cells with over 17% efficiency," vol. 6, p. 1501873, (2016).

[21]   N.-G. J. T. J. o. P. C. L. Park, "Organometal perovskite light absorbers toward a 20% efficiency low-cost solid-state mesoscopic solar cell," vol. 4, pp. 2423-2429, (2013).

[22]   M. Mujahid, C. Chen, W. Hu, Z.-K. Wang, and Y. J. S. R. Duan, "Progress of high- throughput and low- cost flexible perovskite solar cells," vol. 4, p. 1900556, (2020).

[23]   Y. Zhang, Y. Liu, and S. J. A. F. M. Liu, "Composition Engineering of Perovskite Single Crystals for High- Performance Optoelectronics," vol. 33, p. 2210335, (2023).

[24]   E. Smecca, V. Valenzano, S. Valastro, I. Deretzis, G. Mannino, G. Malandrino, *et al.*, "Two-step MAPbI 3 deposition by low-vacuum proximity-space-effusion for high-efficiency inverted semitransparent perovskite solar cells," vol. 9, pp. 16456-16469, (2021).

[25]   Y. Wang, J. Luo, R. Nie, and X. J. E. T. Deng, "Planar perovskite solar cells using CH3NH3PbI3 films: a simple process suitable for large- scale production," vol. 4, pp. 473-478, (2016).

[26]   J. H. Heo, D. H. Shin, M. L. Lee, M. G. Kang, S. H. J. A. a. m. Im, and interfaces, "Efficient organic–inorganic hybrid flexible perovskite solar cells prepared by lamination of polytriarylamine/CH3NH3PbI3/anodized Ti metal substrate and graphene/PDMS transparent electrode substrate," vol. 10, pp. 31413-31421, (2018).

[27]   D. Liu, W. Zha, J. Chen, and R. J. A. P. E. Sa, "Theoretical study of structural stability, electronic and optical properties of MA1− xCsxPbI3 for photovoltaic applications," vol. 13, p. 011007, (2019).

[28]   S. Lim, M. Ha, Y. Lee, and H. J. A. O. M. Ko, "Large- Area, Solution-Processed, Hierarchical MAPbI3 Nanoribbon Arrays for Self- Powered Flexible Photodetectors," vol. 6, p. 1800615, (2018).

[29]   J. Wang, J. Liu, Z. Du, and Z. J. J. o. E. C. Li, "Recent advances in metal halide perovskite photocatalysts: Properties, synthesis and applications," vol. 54, pp. 770-785, (2021).

[30]   Y. Yuan and J. J. A. o. c. r. Huang, "Ion migration in organometal trihalide perovskite and its impact on photovoltaic efficiency and stability," vol. 49, pp. 286-293, (2016).

[31]   C. Altinkaya, E. Aydin, E. Ugur, F. H. Isikgor, A. S. Subbiah, M. De Bastiani, *et al.*, "Tin oxide electron- selective layers for efficient, stable, and scalable perovskite solar cells," vol. 33, p. 2005504, (2021).

[32]   P. Lopez- Varo, J. A. Jiménez- Tejada, M. García- Rosell, S. Ravishankar, G.

Garcia- Belmonte, J. Bisquert, *et al.*, "Device physics of hybrid perovskite solar cells: theory and experiment," vol. 8, p. 1702772, (2018).

[33]   D. Bogachuk, S. Zouhair, K. Wojciechowski, B. Yang, V. Babu, L. Wagner, *et al.*, "Low-temperature carbon-based electrodes in perovskite solar cells," vol. 13, pp. 3880-3916, (2020).

[34]   Q. Wei, Z. Yang, D. Yang, W. Zi, X. Ren, Y. Liu, *et al.*, "The effect of transparent conductive oxide on the performance CH3NH3PbI3 perovskite solar cell without electron/hole selective layers," vol. 135, pp. 654-661, (2016).

[35]   Y. Zhao, W. Zhou, H. Tan, R. Fu, Q. Li, F. Lin, *et al.*, "Mobile-ion-induced degradation of organic hole-selective layers in perovskite solar cells," vol. 121, pp. 14517-14523, (2017).

[36]   Y. Raoui, H. Ez-Zahraouy, N. Tahiri, O. El Bounagui, S. Ahmad, and S. J. S. E. Kazim, "Performance analysis of MAPbI3 based perovskite solar cells employing diverse charge selective contacts: Simulation study," vol. 193, pp. 948-955, (2019).

[37]   M. Zhong, Y. Liang, J. Zhang, Z. Wei, Q. Li, and D. J. J. o. M. C. A. Xu, "Highly efficient flexible MAPbI 3 solar cells with a fullerene derivative-modified SnO 2 layer as the electron transport layer," vol. 7, pp. 6659-6664, (2019).

[38]   D. Jayan K, V. J. A. T. Sebastian, and Simulations, "Comparative study on the performance of different Lead- based and Lead- free perovskite solar cells," vol. 4, p. 2100027, (2021).

[39]   S. P. Dunfield, A. Bojar, S. Cacovich, M. Frégnaux, T. Klein, R. Bramante, *et al.*, "Carrier gradients and the role of charge selective contacts in lateral heterojunction all back contact perovskite solar cells," vol. 2, (2021).

[40]   J. Zhao, X. Zheng, Y. Deng, T. Li, Y. Shao, A. Gruverman, *et al.*, "Is Cu a stable electrode material in hybrid perovskite solar cells for a 30-year lifetime?," vol. 9, pp. 3650-3656, (2016).

[41]   K. D. Jayan, V. J. S. S. Sebastian, and Technology, "Comparative performance analysis of mixed halide perovskite solar cells with different transport layers and back metal contacts," vol. 36, p. 065010, (2021).

[42] S. T. Williams, F. Zuo, C.-C. Chueh, C.-Y. Liao, P.-W. Liang, and A. K.-Y. J. A. n. Jen, "Role of chloride in the morphological evolution of organo-lead halide perovskite thin films," vol. 8, pp. 10640-10654, (2014).

[43] T. Duong, H. K. Mulmudi, H. Shen, Y. Wu, C. Barugkin, Y. O. Mayon, *et al.*, "Structural engineering using rubidium iodide as a dopant under excess lead iodide conditions for high efficiency and stable perovskites," vol. 30, pp. 330-340, (2016).

[44] J. C. Brauer, D. Tsokkou, S. Sanchez, N. Droseros, B. Roose, E. Mosconi, *et al.*, "Comparing the excited-state properties of a mixed-cation–mixed-halide perovskite to methylammonium lead iodide," vol. 152, (2020).

[45] O. Selig, A. Sadhanala, C. Muller, R. Lovrincic, Z. Chen, Y. L. Rezus, *et al.*, "Organic cation rotation and immobilization in pure and mixed methylammonium lead-halide perovskites," vol. 139, pp. 4068-4074, (2017).

[46] Z.-K. Tang, Y.-N. Zhu, Z.-F. Xu, and L.-M. J. P. C. C. P. Liu, "Effect of water on the effective Goldschmidt tolerance factor and photoelectric conversion efficiency of organic–inorganic perovskite: insights from first-principles calculations," vol. 19, pp. 14955-14960, (2017).

[47] F. Mahdi, I. Morteza, and G. M. Ebrahim, "DFT Study of Mechanical Properties and Stability of Cubic Methylammonium Lead Halide Perovskites (CH3NH3PbX3, X= I, Br, Cl)," (2017).

[48] T. Maassen, "'LOOKING INSIDE'A PEROVSKITE," (2022).

[49] Y. Jiang, S. He, L. Qiu, Y. Zhao, and Y. J. A. P. R. Qi, "Perovskite solar cells by vapor deposition based and assisted methods," vol. 9, (2022).

[50] L. K. Ono, M. R. Leyden, S. Wang, and Y. J. J. o. M. C. A. Qi, "Organometal halide perovskite thin films and solar cells by vapor deposition," vol. 4, pp. 6693-6713, (2016).

[51] S. Chen, L. Lei, S. Yang, Y. Liu, Z.-S. J. A. a. m. Wang, and interfaces, "Characterization of perovskite obtained from two-step deposition on mesoporous titania," vol. 7, pp. 25770-25776, (2015).

[52] H. J. A. F. M. Chen, "Two- Step Sequential Deposition of Organometal Halide Perovskite for Photovoltaic Application," vol. 27, p. 1605654, (2017).

[53]   M. Wang, Y. Feng, J. Bian, H. Liu, and Y. J. C. P. L. Shi, "A comparative study of one-step and two-step approaches for MAPbI3 perovskite layer and its influence on the performance of mesoscopic perovskite solar cell," vol. 692, pp. 44-49, (2018).

[54]   B. Xia, Z. Wu, H. Dong, J. Xi, W. Wu, T. Lei, *et al.*, "Formation of ultrasmooth perovskite films toward highly efficient inverted planar heterojunction solar cells by micro-flowing anti-solvent deposition in air," vol. 4, pp. 6295-6303, (2016).

[55]   S. H. Chang, W.-C. Huang, C.-C. Chen, S.-H. Chen, and C.-G. J. A. S. S. Wu, "Effects of anti-solvent (iodobenzene) volume on the formation of CH3NH3PbI3 thin films and their application in photovoltaic cells," vol. 445, pp. 24-29, (2018).

[56]   Y. He, S. Xin, Y. Ren, S. Li, J. He, J. Li, *et al.*, "Effects of anti-solvent temperature on microstructures and photovoltaic properties of TiO2@ MAPbI3 core-shell nanowire arrays," vol. 147, p. 115610, (2023).

[57]   B. Zhang, D. Liu, P. Chen, W. Liu, J. Zhao, H. Li, *et al.*, "Improved perovskite crystallization via antisolvent-assisted processed using additive engineering for efficient perovskite solar cells," vol. 855, p. 157396, (2021).

[58]   H. Li, Y. Xia, C. Wang, G. Wang, Y. Chen, L. Guo, *et al.*, "High-efficiency and stable perovskite solar cells prepared using chlorobenzene/acetonitrile antisolvent," vol. 11, pp. 34989-34996, (2019).

[59]   S. Ghosh, S. Mishra, and T. J. A. m. i. Singh, "Antisolvents in perovskite solar cells: importance, issues, and alternatives," vol. 7, p. 2000950, (2020).

[60]   Y. Zhang, A. Kirs, F. Ambroz, C. T. Lin, A. S. Bati, I. P. Parkin, *et al.*, "Ambient fabrication of organic–inorganic hybrid perovskite solar cells," vol. 5, p. 2000744, (2021).

[61]   Z. Liu, M. Chen, L. Wan, Y. Liu, Y. Wang, Y. Gan, *et al.*, "Anti-solvent spin-coating for improving morphology of lead-free (CH 3 NH 3) 3 Bi 2 I 9 perovskite films," vol. 1, pp. 1-11, (2019).

[62]   C. A. Aranda, L. Caliò, and M. J. C. Salado, "Toward commercialization of stable devices: An overview on encapsulation of hybrid organic-inorganic perovskite solar cells," vol. 11, p. 519, (2021).

[63]   B. Roose, Q. Wang, and A. J. A. E. M. Abate, "The role of charge selective

contacts in perovskite solar cell stability," vol. 9, p. 1803140, (2019).

[64] K. Wang, Z. Jin, L. Liang, H. Bian, D. Bai, H. Wang, *et al.*, "All-inorganic cesium lead iodide perovskite solar cells with stabilized efficiency beyond 15%," vol. 9, p. 4544, (2018).

[65] M. I. Alturisa, J. Wira, and R. Hidayat, "Influences of precursor solution concentration and temperature on CH3NH3PbI3 perovskite layer morphology and the unconverted PbI2 proportion to their perovskite solar cell characteristics," in *Journal of Physics: Conference Series*, (2017), p. 012046.

[66] H. Shahivandi, M. Vaezzadeh, M. J. S. E. M. Saeidi, and S. Cells, "Theory of light-induced degradation in perovskite solar cells," vol. 208, p. 110383, (2020).

[67] L. Elton and D. F. J. A. J. o. P. Jackson, "X-ray diffraction and the Bragg law," vol. 34, pp. 1036-1038, (1966).

[68] J. Marí Guaita, "Different Approaches for Improving the Stability of Hybrid Perovskites," Universitat Politècnica de València, (2023).

[69] X. Li, D. Bi, C. Yi, J.-D. Décoppet, J. Luo, S. M. Zakeeruddin, *et al.*, "A vacuum flash–assisted solution process for high-efficiency large-area perovskite solar cells," vol. 353, pp. 58-62, (2016).

[70] H. S. Jung and N. G. J. s. Park, "Perovskite solar cells: from materials to devices," vol. 11, pp. 10-25, (2015).

[71] T.-L. Wu, J.-K. Tsai, Y.-Z. Song, M.-X. Chen, T.-C. Wu, K.-W. Min, *et al.*, "Influence of molar ratio of MAI and PbI2 on synthesis of perovskite film," vol. 36, p. 2141016, (2022).

[72] Y. Wang, M. Zhong, L. J. S. Chai, and Microstructures, "Effects of the concentration of PbI2 and CH3NH3I on the perovskite films and the performance of perovskite solar cells based on ZnO-TiO2 nanorod arrays," vol. 123, pp. 189-200, (2018).

[73] N.-G. J. M. t. Park, "Perovskite solar cells: an emerging photovoltaic technology," vol. 18, pp. 65-72, (2015).

[74] M. Holt, R. Harder, R. Winarski, and V. J. A. R. o. M. R. Rose, "Nanoscale hard X-ray microscopy methods for materials studies," vol. 43, pp. 183-211, (2013).

[75] A. A. Bunaciu, E. G. UdriŞTioiu, and H. Y. J. C. r. i. a. c. Aboul-Enein, "X-ray

diffraction: instrumentation and applications," vol. 45, pp. 289-299, (2015).

[76] N. Qamhieh, A. Najar, Z. Qamhieh, B. A. Aziz, A. Mansour, and I. J. O. Alghoul, "Synthesis and characterization of a perovskite film for solar cells applications," vol. 171, pp. 648-651, (2018).

[77] P. L. Christiansen, "Current electromagnetic research in Denmark," in (*1973*) *Antennas and Propagation Society International Symposium*, 1973, pp. 208-211.

[78] J. Huang, T. Cavanaugh, and B. Nur, "1 An Introduction to SEM Operational Principles and Geologic Applications for Shale Hydrocarbon Reservoirs," (2013).

[79] H. P. Moeur, A. Zanella, and T. J. J. o. C. E. Poon, "An introduction to UV-vis spectroscopy using sunscreens," vol. 83, p. 769, (2006).

[80] D. A. Czegan and D. K. Hoover, "UV–visible spectrometers: versatile instruments across the chemistry curriculum," ed: ACS Publications, (2012).

[81] M. S. H. Akash and K. Rehman, *Essentials of pharmaceutical analysis*: Springer, (2020).

[82] J. Mellqvist, A. J. J. o. Q. S. Rosén, and R. Transfer, "DOAS for flue gas monitoring—II. Deviations from the Beer-Lambert law for the UV/visible absorption spectra of NO, NO2, SO2 and NH3," vol. 56, pp. 209-224, (1996).

[83] H.-H. Perkampus, *UV-VIS Spectroscopy and its Applications*: Springer Science & Business Media, (2013).

[84] M. Picollo, M. Aceto, and T. J. P. s. r. Vitorino, "UV-Vis spectroscopy," vol. 4, p. 20180008, (2018).

[85] I. Zhaksylykova, "Magneto-optic detection limits for semiconductor spintronics," Université Paris-Saclay (ComUE), (2018).

[86] A. J. S.-S. E. Beer, "The Hall effect and related phenomena," vol. 9, pp. 339-351, (1966).

[87] H. Wen, J. Shah, and R. S. J. I. t. o. b. e. Balaban, "Hall effect imaging," vol. 45, pp. 119-124, (1998).

[88] C. Berthomieu and R. J. P. r. Hienerwadel, "Fourier transform infrared (FTIR) spectroscopy," vol. 101, pp. 157-170, (2009).

[89] F. Higgins and A. J. D. A. T. Rein, "Quantitative analysis of copolymers using

the Cary 630 FTIR spectrometer," (2011).

[90] Z. Bacsik, J. Mink, and G. J. A. S. R. Keresztury, "FTIR spectroscopy of the atmosphere. I. Principles and methods," vol. 39, pp. 295-363, (2004).

[91] L. C. Lee, C.-Y. Liong, A. A. J. C. Jemain, and I. L. Systems, "A contemporary review on Data Preprocessing (DP) practice strategy in ATR-FTIR spectrum," vol. 163, pp. 64-75, (2017).

[92] F. Huth, A. Govyadinov, S. Amarie, W. Nuansing, F. Keilmann, and R. J. N. l. Hillenbrand, "Nano-FTIR absorption spectroscopy of molecular fingerprints at 20 nm spatial resolution," vol. 12, pp. 3973-3978, (2012).

[93] G. R. Kumar, A. D. Savariraj, S. Karthick, S. Selvam, B. Balamuralitharan, H.-J. Kim*, et al.*, "Phase transition kinetics and surface binding states of methylammonium lead iodide perovskite," vol. 18, pp. 7284-7292, (2016).

[94] P. Basumatary and P. J. B. o. M. S. Agarwal, "Two-step fabrication of MAPbI 3 perovskite thin films with improved stability," vol. 42, p. 268, (2019).

[95] O. E. Semonin, G. A. Elbaz, D. B. Straus, T. D. Hull, D. W. Paley, A. M. Van der Zande*, et al.*, "Limits of carrier diffusion in n-type and p-type CH3NH3PbI3 perovskite single crystals," vol. 7, pp. 3510-3518, (2016).

[96] A. El-Naggar, M. Osman, Z. K. Heiba, M. B. Mohamed, A. Kamal, A. Aldhafiri*, et al.*, "Effect of chlorobenzene on the optical and structural properties of CH3NH3PbI3: DMF perovskite films," vol. 14, pp. 287-297, (2021).

[97] G. Abdelmageed, L. Jewell, K. Hellier, L. Seymour, B. Luo, F. Bridges*, et al.*, "Mechanisms for light induced degradation in MAPbI3 perovskite thin films and solar cells," vol. 109, (2016).

[98] X. Hou, S. Huang, W. Ou-Yang, L. Pan, Z. Sun, X. J. A. a. m. Chen*, et al.*, "Constructing efficient and stable perovskite solar cells via interconnecting perovskite grains," vol. 9, pp. 35200-35208, (2017).

[99] A. Sharma and N. Chaure, "Studies on CH3NH3PbI3 prepared by low-cost wet chemical technique," *Applied Physics A,* vol. 125, 10/17 (2019).